`Tandem`: An Open-Source High-Performance Computing Volumetric Software to Model Sequences of Earthquakes and Aseismic Slip Across Complex Fault Systems

Alice-Agnes Gabriel (algabriel@ucsd.edu)[1,2], Piyush Karki (piyush.karki@lmu.de)[2], Yohai Magen (ymagen@ucsd.edu)[1], Bar Oryan (boryan@ucsd.edu)[1], Thomas Ulrich (thomas.ulrich@lmu.de)[2], Jeena Yun (j4yun@ucsd.edu)[1], and Dave A. May (dmay@ucsd.edu)[1]

[1]Institute of Geophysics and Planetary Physics, Scripps Institution of Oceanography, University of California at San Diego, 9500 Gilman Drive La Jolla, CA 92093-0225, USA.

[2]Geophysics, Department of Earth and Environmental Sciences, Ludwig-Maximilians-Universität (LMU) München, Theresienstraße 41, 80333 Munich, Germany.

Corresponding author: Alice-Agnes Gabriel

Institute of Geophysics and Planetary Physics

Scripps Institution of Oceanography, University of California San Diego

9500 Gilman Drive, La Jolla, CA 92093-0225, USA.

Email: algabriel@ucsd.edu

Abstract. Simulating sequences of earthquakes and aseismic slip (SEAS) on realistic fault systems provides a physical framework to understand the evolution of the seismic cycle, but remains computationally expensive. Volumetric approaches offer the physical flexibility to handle complex geometries and heterogeneous off-fault media but may incur prohibitively high computational costs when applied to the vast range of spatial and temporal scales inherent to earthquake cycles. This paper documents developments in `Tandem`, an open-source volumetric SEAS simulation software that addresses these challenges using a symmetric interior penalty discontinuous Galerkin formulation on unstructured curvilinear meshes in 2D and 3D with high-order polynomial basis functions. We describe `Tandem` from a user's perspective, covering mesh formats, checkpointing, model configuration via human-readable files, and flexible loading schemes for various tectonic settings. To lower barriers to usage, `Tandem` is distributed as a standalone C++/PETSc code, a pre-configured virtual machine image, and as an application on the Quakeworx Science Gateway, where users can run simulations without installing dependencies or securing direct HPC access. We report on practical development choices of interest to SEAS- and other scientific software-developers. To mitigate the cost of volumetric discretization, the software provides both matrix-free and assembled-matrix formulations with a fully volumetric explicit approach utilizing hybrid geometric–algebraic multigrid preconditioners, and a Discrete Green's Function mode that accelerates time-stepping by precomputing traction kernels. We document performance on both CPU and GPU supercomputers, including near-ideal weak scaling up to 112,000 MPI ranks on the supercomputer Frontera. Finally, as demonstration examples, we present validation in a 3D SEAS community benchmark (BP7) and a 2D example examining how off-megathrust material heterogeneity influences seismic cycle behavior. By sharing software design choices as well as practical guidance for its use, we hope to make volumetric HPC-driven SEAS modeling more accessible to the earthquake science community.

1 Introduction

Natural fault systems slip across a wide range of timescales, from creep lasting centuries, to transient slow-slip events and afterslip lasting weeks to months, to earthquakes rupturing in seconds (e.g., Helmstetter and Shaw, 2009; Obara and Kato, 2016; Bürgmann, 2018; Lavier et al., 2021; Meade, 2024; Gabriel et al., 2024). Numerical simulations of sequences of earthquakes and aseismic slip, termed "SEAS" models, (e.g., Erickson et al., 2020), aim to capture the complete seismic cycle in a self-consistent, physics-based modeling approach (e.g., Rice and Tse, 1986; Kato, 2002; Barbot et al., 2012).

SEAS models unify earthquake system mechanics by integrating the interseismic phase, spontaneous earthquake nucleation, co-seismic rupture propagation, and post-seismic relaxation. They provide a useful framework to explore faulting physics across multiple spatial and temporal scales and to connect long-term tectonic deformation, expressed through fault zone rheology, and stress states, with short-term seismic and transient slip events. SEAS models also enable studying how various

physical processes, such as fault damage zones (Abdelmeguid and Elbanna, 2022), fluid diffusion (Zhu et al., 2020), viscoelasticity (Allison and Dunham, 2018) or anisotropy (Mckay et al., 2019), impact seismicity and fault slip behavior, with important implications for seismic hazard (Lambert and Lapusta, 2021).

Several numerical methods have been developed to simulate SEAS problems, each with strengths and limitations. Boundary element implementations, such as the boundary element and (spectral) boundary integral methods (BEM/BIM), are highly efficient because they reduce the dimensionality of the problem. These methods have been applied to quasi-dynamic and fully dynamic earthquake sequence simulations in both two- and three-dimensional (2D and 3D) settings (e.g., Liu and Rice, 2005; Segall and Bradley, 2012; Bradley, 2014; Li and Liu, 2016; Barbot, 2019; Lapusta et al., 2000; Romanet and Ozawa, 2022; Herrera et al., 2024). Beyond purely elastic bulk assumptions, boundary-integral formulations have been extended to include *off-fault* material response by coupling fault slip to distributed anelastic deformation via boundary–volume (Green's-function) kernels, enabling viscoelastic lithosphere–asthenosphere coupling and rheological consistency (Lambert and Barbot, 2016; Mallick et al., 2022; Shi et al., 2022). Recently, hierarchical BIM approaches use H-matrix acceleration (Börm et al., 2003) to reduce the computational cost of evaluating dense stress-interaction matrices in large-scale SEAS simulations, enabling three-dimensional problems and more complex fault geometries to be incorporated (Ozawa et al., 2023; Cheng et al., 2025). However, BEM/BIM methods may generally struggle to represent complex fault system and domain geometries or varying material properties and rheologies, despite recent advances (Romanet et al., 2025).

Volumetric approaches, such as finite-difference and finite-element methods (Aagaard et al., 2013; Almquist and Dunham, 2021; Luo et al., 2020), are computationally more demanding but can address these challenges. Finite-difference approaches discretize the model domain using a structured grid, enabling efficient computation (Erickson and Dunham, 2014; Erickson et al., 2017; Allison and Dunham, 2018; Harvey et al., 2023; Sun and Zhang, 2025) but are less suitable to model (i) domains with irregular boundaries, (ii) problems with complex fault systems, and (iii) domains with highly heterogeneous material properties. Finite-element methods, including spectral element and discontinuous Galerkin formulations, offer greater flexibility in representing fault complexity, heterogeneous material properties, and versatile boundary conditions (Kaneko et al., 2011; Uphoff et al., 2023; Yun et al., 2025b). Hybrid solvers that combine multiple methods (Ma et al., 2019; Mia et al., 2022) leverage the strengths of different numerical schemes but often require intricate coupling techniques.

Community code-comparison efforts (Erickson et al., 2020, 2023; Jiang et al., 2022; Lambert et al., 2025) have verified many SEAS methods on idealized benchmark problems, with excellent agreement on canonical tests. However, important challenges remain. SEAS simulations are now among the most computationally demanding problems in geophysics, especially when integrating multi-physics processes such as fluid flow (e.g., Perez-Silva et al., 2023). This is because they must resolve spatial

scales from critical nucleation sizes to fault-zone widths to plate boundaries, and time scales from milliseconds during dynamic rupture to centuries and millennia over seismic cycles, requiring numerical methods that can adapt across disparate timescales (e.g., Lambert and Lapusta, 2021). Achieving adequate resolution across these scales, particularly in 3D simulations, is computationally demanding. Hence, SEAS models often remain small enough to run efficiently by limiting their dimensionality, overall size, or the range of physical parameters considered. Other than a few notable exceptions (e.g., Liu et al., 2020; Ozawa et al., 2023; Uphoff et al., 2023; Chen et al., 2024), adoption of HPC infrastructure, which can overcome these challenges, has remained limited within the SEAS community. Moreover, FAIR-compliant data and workflow practices (Wilkinson et al., 2016) for preprocessing, postprocessing, and visualization are still in early stages of adoption. Bridging this gap requires accessible software as well as targeted educational initiatives that deliver research-grade software training (Denolle et al., 2025). In this study, we document `Tandem`[1] from a user's perspective. `Tandem` is an open-source software designed for simulating sequences of earthquakes and aseismic slip in 2D and 3D. It leverages the flexibility and accuracy of the Symmetric Interior Penalty discontinuous Galerkin (SIPG, Arnold et al. (2002); Rivière (2008)) finite-element method, which enables robust handling of complex geometries, heterogeneous material properties, and nonlinear frictional behavior. This enables native representation of intersecting, branching, non-planar faults, heterogeneous material properties, and topography. Continuous integration, regression tests, and online documentation support reproducible modeling and community contributions.

2 Numerical Method

2.1 Governing equations

In SEAS models, predefined fault interfaces obey a rate- and state-dependent friction law, which describes frictional sliding for many rock types in laboratory experiments (Dieterich, 1979; Ruina, 1983; Dieterich and Kilgore, 1994). We summarize the governing equations in Appendix A. `Tandem` assumes linear elasticity in the fault-surrounding medium (Uphoff et al., 2023) and computes the mechanical domain response to the on-fault displacement discontinuity and sets shear and normal traction in the rate-and-state friction constitutive relation.

In quasi-dynamic simulations, we solve a time-dependent coupled system of differential equations consisting of (i) the elliptic partial differential equation (PDE) for the elasticity problem of the bulk (with a radiation-damping term, Rice (1993); Cochard and Madariaga (1994); Lapusta et al. (2000)), and (ii) two ordinary differential equations (ODEs) for the rate-and-state friction variables (e.g., Rice, 1993) at each point across the fault. In fully dynamic simulations, the bulk PDEs in (i) are

[1] https://github.com/TEAR-ERC/tandem

elastodynamic (i.e., hyperbolic). In this paper, we focus on the quasi–dynamic version of *Tandem*, which has been extensively verified and benchmarked in recent SEAS community code comparison efforts (Erickson et al., 2023; Lambert et al., 2025).

2.2 Symmetric Interior Penalty discontinuous Galerkin (SIPG) method

Discontinuous Galerkin (DG) methods are increasingly used in seismology to model wave propagation, earthquake dynamic rupture, and related problems that require solving hyperbolic PDEs (e.g., Hesthaven and Warburton, 2008; Reinarz et al., 2020; Moczo et al., 2021; Igel, 2017; Krenz et al., 2023). Owing to the spatially local character of their discrete high-order accurate discrete operators, DG schemes support boundary-conforming curvilinear meshes (Warburton, 2013) and unstructured meshes composed of triangles and tetrahedra, which facilitates the representation of complex geological structures and topography (e.g., Mercerat and Glinsky, 2015; Gabriel et al., 2021). The use of numerical fluxes, without enforcing field continuity across element boundaries, enables to naturally treat non-linear interface conditions (e.g., Tago et al., 2012; Pelties et al., 2012). Recent DG applications in seismology have increasingly exploited large-scale HPC infrastructure (e.g., Wilcox et al., 2010; Heinecke et al., 2014), benefiting from on-node hardware optimizations. `Tandem` extends the DG framework to SEAS problems by discretizing the elastostatic problem, that is, an elliptic PDE (Appendix A).

`Tandem` uses a specific "flavor" of DG, the Symmetric Interior Penalty DG (SIPG) formulation (Rivière, 2008; Uphoff et al., 2023). In SIPG, numerical penalty terms are introduced to weakly impose Dirichlet boundary conditions, and weakly enforce inter-element continuity of the displacement field where no faults are present (Fig. 1a). When a fault is present, the enforcement of a continuous displacement field is removed (i.e., the penalty term is not used) and the discontinuity (jump) in the displacement in the fault parallel direction is defined from the friction law, whilst the jump in displacement normal to the fault is enforced to be zero. SIPG results in a symmetric operator and is provably stable, provided that the penalty is chosen large enough. Because in SIPG continuity is enforced weakly, models can natively handle discontinuities such as faults and other internal interfaces. SIPG supports unstructured meshes in two (triangles) and three (tetrahedra) dimensions (Fig. 1b,c), enabling local mesh refinement while keeping the domain large enough to approximate whole-space boundary conditions (Jiang et al., 2022; Lambert et al., 2025). High-order polynomial bases (`Tandem` supports arbitrary orders) and curvilinear (non-affine) meshes allow complicated geometries to be represented with high accuracy. SIPG also handles sub-element variations in material properties.

The SIPG discretization is a computationally expensive approach (Kirby et al., 2012) for SEAS – primarily due the large system of linear equations, associated with the elastostatic problem, which needs to be frequently solved. We alleviate the burden of the solve cost by using preconditioned Krylov (iterative) solvers. As the continuous problem is an elliptic PDE, and

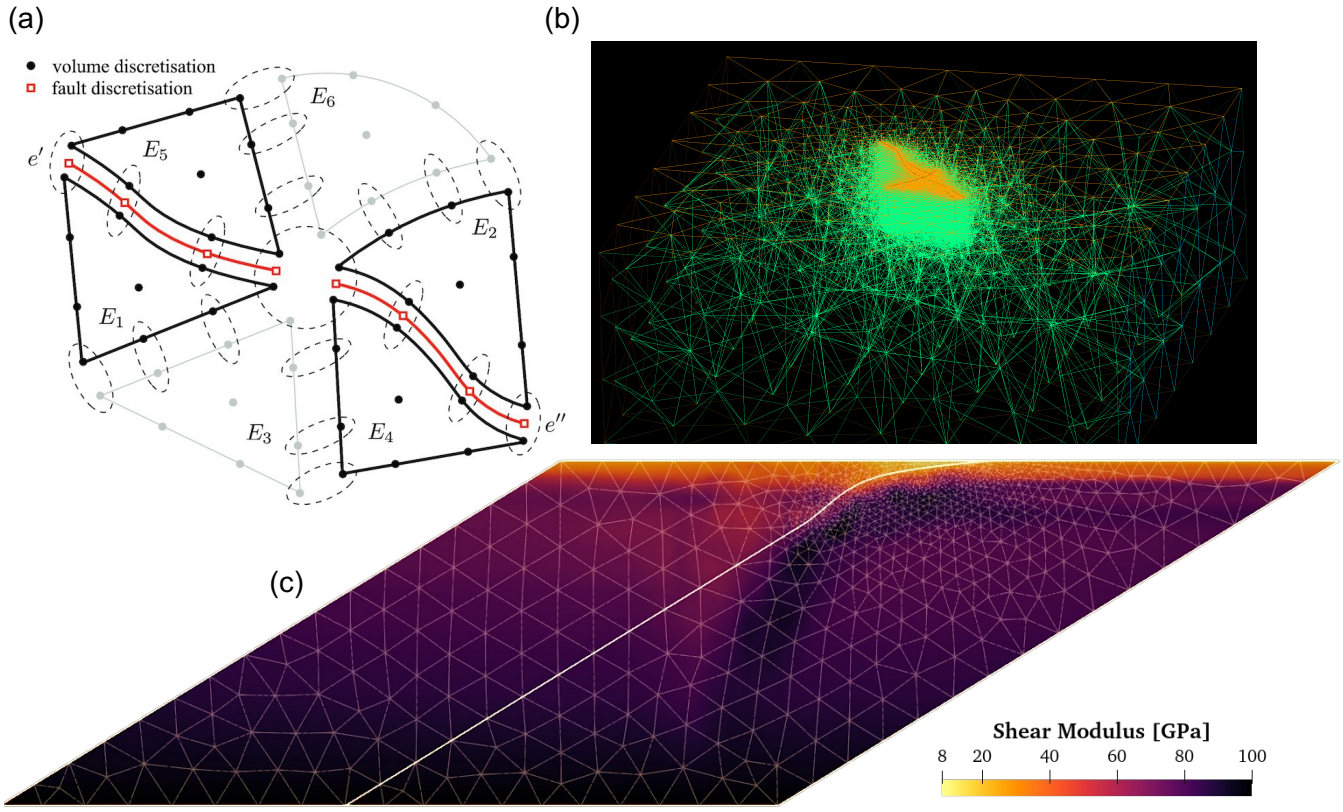

Figure 1. (a) Symmetric Interior Penalty discontinuous Galerkin (SIPG) representation of a SEAS problem. To emphasize the discontinuous nature of the discontinuous Galerkin (DG) representation and the penalty weak coupling across facets, cells and facets are sketched as disjoint; the dashed loops enclose facet basis functions between adjacent cells functions (and across faults) which are collocated in space. (b) Gmsh (Geuzaine and Remacle, 2009) screenshot of a 3D unstructured tetrahedral mesh for the 2019 Ridgecrest, CA, fault system with local refinement near the faults. The element edge length is 250 m at the fault interfaces, gradually coarsening to 20 km toward the domain boundary. This mesh contains 421,154 tetrahedra. (c) 2D unstructured triangular mesh representing the Northern Hikurangi subduction zone, New Zealand (12,160 triangular elements). Colors represent heterogeneous shear modulus (Eberhart-Phillips et al., 2020), which can be represented on the subelement level. (a,b) adapted from Uphoff et al. (2023).

Alt text: Conceptual and practical examples of DG-based SEAS discretization: a schematic of how neighboring elements are weakly coupled across facets while permitting displacement discontinuities across faults; a 3D unstructured tetrahedral mesh for the Ridgecrest fault system refined near faults; and a 2D subduction-zone mesh in which shear modulus varies spatially to represent elastic heterogeneity.

the SIPG discretization is symmetric, we can exploit robust multi-level preconditioners (e.g., two-level domain-decomposition, algebraic multigrid, geometric multigrid). Such preconditioners are suitable for modern domain-decomposition and multilevel preconditioners (Rudi et al., 2015; Fehn et al., 2020), which are essential for large-scale SEAS simulations which require a large number of time-steps, on the order of millions. Leveraging these algorithmic properties of the SIPG formulation together with optimized kernels for evaluating the SIPG linear and bilinear forms, `Tandem` is inherently parallel and well suited for high-resolution SEAS simulations on large-scale distributed memory architectures (Uphoff et al., 2023).

3 Implementation

The SIPG-based SEAS formulation in `Tandem` yields very large discrete systems and expensive sparse linear solves, particularly in 3D at high polynomial degree. Thus, the code is designed for efficient large-scale runs on modern HPC architectures with performance-portable CPU and GPU back ends. At the same time, it supports dimension-independent workflows in 2D and 3D and provides a user interface that makes it easy to build, test, and share SEAS models.

3.1 Software design choices and parallelization

`Tandem`[2] is implemented in `C++17` as a modular library with application front-ends (executables) for elastostatic problems (executable named `static`) and quasi-dynamic SEAS simulations (executable named `tandem`). The same discretization and solver infrastructure is used for both the elastostatic solves and the time-dependent SEAS application, which simplifies verification and maintenance. Parallelism is provided through MPI (Walker and Dongarra, 1996), with distributed-memory domain decomposition of the unstructured mesh, and through optional GPU acceleration.

To accommodate the expensive volumetric discretization, `Tandem` offers both matrix-free and assembled-matrix formulations of the SIPG operators. Matrix-free operators reduce memory requirements and can improve cache efficiency at high polynomial degrees, while assembled sparse matrices are convenient for some preconditioners and direct solvers. A typical seismic cycle simulation requires $\mathcal{O}(10^6)$ elliptic solves for the displacement. Algorithmic efficiency and parallel scalability are crucial requirements for any solver for 2D and especially 3D simulations For large-scale problems, `Tandem` employs a hybrid geometric-algebraic multigrid preconditioner (May et al., 2015; Rudi et al., 2015). Multigrid preconditioners are algorithmically optimal, amenable to highly scalable parallel implementations (Rudi et al., 2015), and are effective with high-order continuous Galerkin methods (Rønquist and Patera, 1987) and discontinuous Galerkin discretizations (Fehn et al., 2020).

[2] https://github.com/TEAR-ERC/tandem

Access to both sparse direct factorizations and geometric-algebraic multigrid preconditioners are realized via the Portable, Extensible Toolkit for Scientific computation (PETSc, Balay et al., 1997, 2015, 2021; Abhyankar et al., 2014; Amestoy et al., 2001, 2006), which `Tandem` uses for scalable linear and nonlinear solvers, time integration, and preconditioning. PETSc supports MPI and GPU through CUDA, HIP, Kokkos, or OpenCL backends, as well as hybrid MPI–GPU parallelism, allowing `Tandem` to target a wide range of CPU-only and heterogeneous CPU-GPU systems without changing application-level code.

Performance-critical local kernels for evaluating DG bilinear and linear forms are generated using YATeTo (Uphoff and Bader, 2020), which is also used in the wave propagation and earthquake dynamic rupture code SeisSol (Gabriel et al., 2025)[3]. YATeTo enables architecture-specific matrix-matrix and tensor contractions, optionally leveraging libraries such as `libxsmm`, and has been demonstrated to achieve a large fraction of peak performance on current petascale systems (Heinecke et al., 2014; Uphoff et al., 2017; Krenz et al., 2021). `Tandem` thus inherits a performance-portable, kernel-based design. The high-level DG formulation is expressed once, and code generators plus PETSc backends specialize it to different node architectures and accelerator backends. The unstructured meshes are distributed across MPI ranks using graph-partitioning libraries such as METIS and ParMETIS (Karypis and Kumar, 1998), which are included among the core dependencies. The resulting partitioning determines ownership of elements and facets. Inter-partition communication is handled through PETSc's distributed vectors and matrices.

3.2 Dimension independence and configuration

`Tandem` is designed to be dimension-independent. The same code base supports both 2D and 3D simulations. Dimension and polynomial degree are selected at compile time using CMake configuration options, which control kernel generation. This approach allows the compiler and YATeTo to aggressively optimize dimension-specific kernels, while users interact with a unified workflow. Low-order and high-order discretizations are thus treated consistently, and both benefit from the same solver and I/O infrastructure. Spatially varying material and friction parameters, as well as boundary conditions and loading histories, are defined in a Lua script[4].

The simulation configuration is based on a combination of human-readable parameter files (TOML, (Prescott-Werner and TOML Community)) and embedded scripting via Lua (Ierusalimschy et al., 1996) and PETSc options. A TOML configuration file stores parameters such as the mesh file, the Lua script defining the model setup, and output and checkpoint settings, and is passed to the executable at run time. This separation allows users to express complex spatial dependence and experiment with different physical setups while keeping the core solver code unchanged. The Lua interface provides a lightweight, flexible

[3] https://github.com/SeisSol/SeisSol/

[4] See the `tandem` documentation at https://tandem.readthedocs.io for detailed examples

and expressive mechanism for defining spatio-temporal material properties, loading and boundary conditions without requiring recompilation.

3.3 Support for discrete Green's functions

Application flexibility and efficiency are provided within `Tandem` by optionally defining the displacement evaluation via a discrete (numerically evaluated) Green's function approach (e.g., van Driel et al., 2015), exploiting advantages of both the boundary integral and volumetric methods (for details see Uphoff et al. (2023)). The optional discrete Green's functions are evaluated once in a pre-computation stage using algorithmically optimal and scalable sparse parallel solvers and multigrid preconditioners, as detailed in the next sections. Once computed, these Green's functions map on-fault slip directly to traction, so subsequent SEAS time steps only require dense operator applications on the fault instead of repeated volumetric solves. This makes the optional Green's function approach particularly advantageous for simpler simulations with many time steps, at the expense of increased memory usage to store the precomputed operators.

3.4 Geometry, meshing, and curvilinear representation

Geometric flexibility is a central design feature of `Tandem` (Fig. 1). The code operates on unstructured triangle and tetrahedral meshes with curvilinear elements, allowing it to represent curved faults, topography, and other complex geological structures with high fidelity. In practice, meshes are typically generated with any version of Gmsh (Figs. 1b,c; Geuzaine and Remacle (2009)), which provides both a CAD engine (via OpenCASCADE[5]) and mesh generation capabilities. Users build geometry and meshing scripts in Gmsh's own language, its python backend or using its graphical interface, specify physical groups to mark faults, free surfaces, and Dirichlet boundaries. They export the created mesh using the Gmsh file format `.msh`, including high-order nodes on curved boundaries. The ASCII `.msh` file format versions ≥ 2 and < 3 are supported natively by `Tandem`. In addition, the code can read in meshes in `.xdmf` + `.h5` file format which allows linking to other community codes such as SeisSol. Physical groups are translated into boundary-conditions and frictional fault interfaces within the DG formulation. The SIPG discretization in `Tandem` supports arbitrary polynomial order on these (possibly non-affine) elements, enabling high-order geometric representation and strong sub-element variation in material properties.

SEAS simulations need to resolve the minimum of the process zone size Λ_0 and the critical nucleation length L_∞ (Rice, 1993; Erickson et al., 2020; Jiang et al., 2022; Day et al., 2005). In the DG setting, this criterion should be interpreted in terms of the effective cell size associated with the polynomial basis: utilizing high-order polynomial bases reduces the effective cell size and thus allows larger apparent element edge lengths for a given on-fault resolution.

[5]https://github.com/Open-Cascade-SAS

3.5 Flexible loading methods

Since `Tandem` utilizes volume discretizations within a finite computational domain, it enables flexible loading conditions that allow spatiotemporal variations. `Tandem` supports three types of boundary conditions: (i) fault governed by a rate-and-state friction law, (ii) a free surface (zero traction) boundary, or (iii) a Dirichlet boundary where the displacement is prescribed. Along Dirichlet boundaries, the user prescribes a spatiotemporal displacement vector, e.g., $\mathbf{u}^D(x,y,t)$ in 2D or $\mathbf{u}^D(x,y,z,t)$ in 3D for time t and spatial coordinates x, y, and z. On Dirichlet boundaries located within the interior of the domain, `Tandem` uses the prescribed value of $\mathbf{u}^D$ to define the jump in displacement across the interface. Below, we present a few exemplary loading methods for 2D subduction zone simulations, highlighting `Tandem`'s flexibility in loading.

The first example is using a parallelogram-shaped domain that is sheared along a uniform dip with a magnitude of half plate convergence rate, $V_p/2$ (Fig. 2a). For example, a 30° fault dipping toward the positive x direction would yield $\mathbf{u}^D(x,y,t) = (\pm V_p t/2 \cos 30^\circ, \mp V_p t/2 \sin 30^\circ)$, where the upper (lower) signs apply to the footwall (hanging wall). This loading method mimics backslip loading (Savage, 1983) and has been utilized to solve the SCEC community benchmark problem BP3, in which `Tandem`'s results show good consistency with other community codes (Erickson et al., 2023).

Another example is horizontal compression from far-field edges (Fig. 2b), similar to the previous study using `Tandem` investigating the effect of slab curvature in subduction zone seismic cycles (Biemiller et al., 2024). The imposed displacements are expressed as $\mathbf{u}^D(x,y,t) = (\pm V_p t/2, 0)$, where the plus (minus) sign applies to the footwall (hanging wall).

`Tandem` can also impose a boundary condition where slab convergence is fully accommodated beneath the slab, e.g., $\mathbf{u}^D(x,y,t) = (V_p t \cos 30^\circ, -V_p t \sin 30^\circ)$, while fixing the motion on the overriding plate (Fig. 2c). This loading resembles the kinematic slab-pull motion observed at subduction zones (Chapple and Tullis, 1977; Forsyth and Uyeda, 1975).

3.6 Continuous integration, continuous development, and documentation

`Tandem` features a continuous integration (CI) and continuous development (CD) infrastructure, which enhances the development workflow by combining automated code-quality checks with thorough testing, reflecting best practices in scientific software engineering. The CI/CD pipeline performs several automated tasks, including checking code formatting, compiling and testing the code across multiple modern compilers (including GCC and Clang), and executing unit and regression tests. The test suite comprises regression tests: (i) for the elastostatic solver in 2D and 3D; (ii) for SEAS tests in 2D; (iii) for parallel consistency checks in both 2D and 3D; and (iv) which verify the theoretical convergence rate (i.e. the relationship between the cell size and spatial discretization error) of the SIPG spatial discretization.

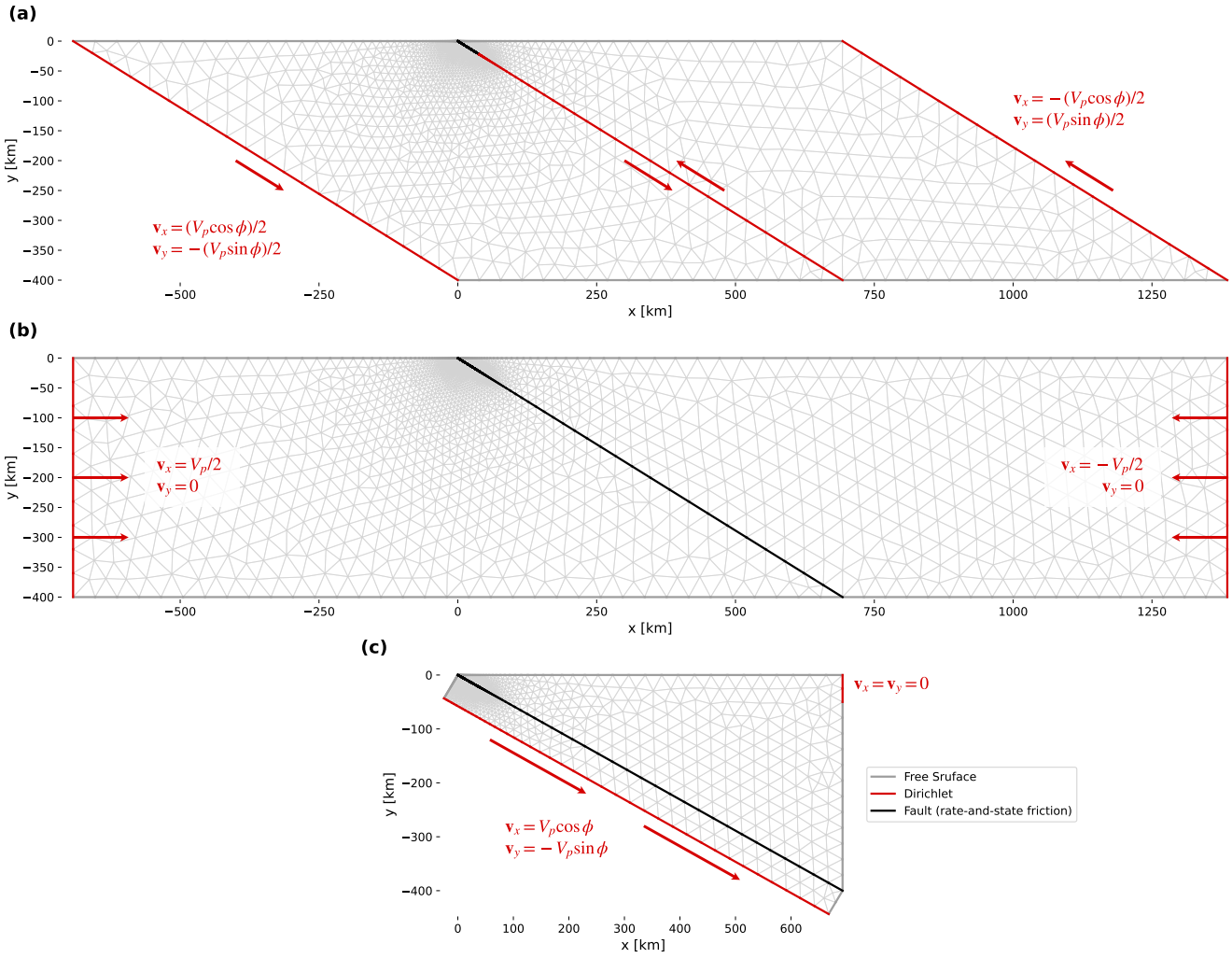

224 **Figure 2.** Examples of loading methods for a planar reverse fault model dipping at 30°. Black, grey, and red lines mark the three boundary
225 conditions of `Tandem`, the fault governed by the rate-and-state friction, the free surface, and the Dirichlet boundaries, respectively. Red
226 arrows indicate the imposed displacement vectors along Dirichlet boundaries. Light grey lines show triangular cells with gradually increasing
227 sizes towards the domain boundary.

Alt text: Three alternative kinematic loading prescriptions for a dipping megathrust model, showing which boundaries are fixed, traction-free, or displacement-controlled and the direction of imposed plate-motion vectors. The panels distinguish backslip-style shearing, far-field horizontal shortening, and a case where convergence is accommodated beneath the slab while the overriding plate remains fixed; mesh coarsening illustrates how resolution is concentrated near the fault.

The CI/CD pipeline is implemented using container-based workflows, which support cross-platform compatibility and provide ready-to-use binaries that behave consistently across different machines and operating systems. This approach simplifies development on diverse HPC environments by decoupling the software stack from the underlying system modules, and it ensures that proposed changes are automatically validated against a broad set of configurations and problem classes.

User-facing documentation is hosted online and built from the same repository. It includes installation guides, detailed descriptions of configuration files, tutorials for building SEAS models (including mesh generation with Gmsh and Lua scripting), and reference material on equation scaling and sign conventions. Combined with the open-source BSD 3-Clause license, this infrastructure lowers the barrier to entry for new users and fosters reproducibility and community contributions.

3.7 Overview of new functionality

Compared to the theoretically focused description of `Tandem` in Uphoff et al. (2023), several key capabilities have been added or substantially extended, broadening the range of SEAS problems that can be tackled on modern HPC systems.

First, `Tandem` now supports scalable checkpointing of discrete Green's functions (Sec. 3.3). In SEAS simulations using the discrete Green's function (DGF) mode, Green's functions are computed in a pre-computation stage and stored in a matrix. In D dimensions with N^f fault basis functions located at $\mathbf{x}_i^f, i = 1, \ldots, N^f$ the DGF matrix has $D \times N^f$ rows and $(D-1) \times N^f$ columns. Each column j represents the displacement (response) $\mathbf{u}(\mathbf{x}_j^f)$ to a unit slip vector at each fault point $\mathbf{x}_j^f$. These Green's function matrix is incrementally assembled, and partial results are periodically written to disk as checkpoints. Each checkpoint records not only the partially assembled matrix but also the mapping information between degrees of freedom and MPI ranks. If the MPI communicator size at restart differs from the original one, the Green's functions are repartitioned using permutation matrices so that the simulation can continue with a different number of MPI ranks. The displacement solution associated with a given set of boundary conditions is checkpointed alongside the DGF matrix, allowing recovery of essential boundary conditions without recomputation. This design enables large DGF computations to be split into smaller segments and run under varying HPC queue and allocation constraints.

Second, a robust time-integration checkpointing system has been implemented for SEAS simulations. These simulations often involve a very large number of time steps and can be limited by maximum wall-time on HPC systems. The checkpointing mechanism periodically writes the complete state of the time integrator to disk (state variable and slip rate), including the current solution vector, internal Runge–Kutta stage data, and relevant PETSc TS solver state. Checkpoints can be triggered based on time-step counter, elapsed CPU time, or physical simulation time, and multiple checkpointed states can be retained.

Simulations can be restarted exactly from any checkpoint file, allowing long simulations to be decomposed into a sequence of shorter jobs that fit within HPC scheduling policies.

Third, the friction-law implementation has been extended and optimized. `Tandem` now supports both the aging law and slip law formulations of rate-and-state friction (Dieterich, 1979; Ruina, 1983). The new slip law implementation is validated through the community benchmark problem BP6, showing good agreement with other community codes (Lambert et al., 2025).

Fourth, `Tandem` now supports the perturbation of normal and shear stresses during a SEAS simulation by updating the background shear ($\boldsymbol{T}^0$) and normal (σ_n^0) stresses at a given time t:

$$\sigma_n(\boldsymbol{x},t) = \sigma_n^0(\boldsymbol{x}) + \hat{\sigma}_n(\boldsymbol{x},t) - \boldsymbol{n}^T\boldsymbol{\sigma}(\mathbf{u})\boldsymbol{n} \tag{1}$$

$$\boldsymbol{T}(\boldsymbol{x},t) = \boldsymbol{T}^0(\boldsymbol{x}) + \hat{\boldsymbol{T}}(\boldsymbol{x},t) + \boldsymbol{B}^T\boldsymbol{\sigma}(\mathbf{u})\boldsymbol{n} \tag{2}$$

where $\boldsymbol{B}$ is the orthonormal basis of tangential directions on the fault, $\boldsymbol{\sigma}$ is the Cauchy stress, $\boldsymbol{n}$ is the unit normal on internal fault boundaries, and $\hat{\boldsymbol{T}}$ and $\hat{\sigma}_n$ are the shear and normal stress perturbations (for detailed definitions see Appendix A). Together with the time-integration checkpointing feature, this allows `Tandem` to model injection-induced pore-fluid pressure variation (Lambert et al., 2025) and fault slip triggering problems (Yun et al., 2025a).

Next, to reduce the cost of the non-linear solve for fault slip-velocity, the rate-and-state root-finder has been reformulated to solve for the logarithm of the slip rate rather than the slip rate itself. This simple reparameterization improves numerical robustness and yields an approximate 30% speed-up in the time-stepping loop for typical SEAS setups, without changing the underlying physical model.

Finally, to alleviate I/O bottlenecks in large-scale simulations, we have implemented a new HDF5-based (The HDF Group) output module in `Tandem`. Previously, extracting quantities such as seismic moment rate over portions of the fault required processing volumetric VTU files (Schroeder et al., 1998) or large collections of CSV probe files, which stress file system limits and are inefficient for monitoring many elements over many time steps. The new I/O module computes and writes the moment rate directly during the simulation, operating inside the rate-and-state kernel where slip rates and state variables are already available. At each time step, the moment-rate contribution is evaluated as $\dot{M} = \int_{dA} \mu V(t)\, dA$, with μ the shear modulus, A the fault length (2D) / area (3D) obtained from exact quadrature weights, and $V(t)$ the slip rate. Elementwise contributions are written in parallel to HDF5 using chunking and collective I/O, preserving numerical accuracy through consistent quadrature and enabling scalable output. The same approach has been extended to fault and domain probe outputs, allowing field data at many probe locations to be stored in a single self-contained HDF5 file.

4 Running `Tandem`

This section provides practical guidance on how to run Tandem simulations using cloud and HPC infrastructure, scaling plots useful for allocation requests on several target machines/infrastructure.

4.1 On a personal device, standalone or via a virtual machine

`Tandem` is distributed as a standalone C++/PETSc code and will run on a personal computer or laptop, if all dependencies are satisfied. The full list of dependencies and installation instructions is documented in `Tandem`'s repository README and installation documentation[6]. The code is also available as a preconfigured virtual machine image that runs out of the box on macOS systems using UTM, providing full compatibility with ARM-based processors. This setup allows users to run `Tandem` simulations directly on their personal laptops without installing dependencies or configuring a development environment (Oryan, 2024). We included both examples presented in Sec. 5 in the current virtual machine image.

4.2 As a Quakeworx App

`Tandem` is deployed as an "App" on the Quakeworx Science gateway[7] (Barker et al., 2019; Chourasia et al., 2024), an open-access platform designed to make advanced seismic modeling broadly accessible. Quakeworx provides a centralized, web browser-based environment where users can run `Tandem` without installing the code, compiling dependencies, or securing access to an HPC system. The `Tandem` Quakeworx App supports three workflows: 2D, 3D, and "autoTandem". In the 2D and 3D modes, users upload their own unstructured mesh and configuration files, select computational resources, and launch simulations in a workflow similar in essence to running `Tandem` on a local cluster. At the same time, the graphical user interface streamlines setup, submission, and job monitoring, eliminating the overhead of environment configuration and HPC system management.

The autoTandem App offers an even lower barrier to entry by providing users with a simplified 2D seismic cycle model scenario and automating many modeling steps, including mesh and input file generation. Users are free to alter a small number of physical parameters, such as dip angle, normal stress, and frictional property distributions via the Quakeworx app interface. This enables new and novice users to explore SEAS models (and Quakeworx) without requiring meshing tools, scripting interfaces, or a full understanding of `Tandem`'s configuration structure. autoTandem also performs internal resolution checks to verify that the chosen discretization is consistent with SEAS accuracy requirements (Sec. 3.4). In addition, autoTandem generates a suite of diagnostic plots that help users visualize their simulations and interpret the resulting fault behavior, further

[6] https://tandem.readthedocs.io/en/latest/getting-started/installation.html
[7] https://quakeworx.org

facilitating education in SEAS modeling. `Tandem` Quakeworx examples are provided in the training GitHub repository[8] and have been utilized in training workshops and teaching.

4.3 On many compute nodes

In Fig. 3a, we report weak-scaling results of the elastostatic solver (executable `static`) on the CPU-based supercomputer Frontera (TACC) using sub-domains containing approximately 1000 P_4 DG elements. Frontera consists of 8,289 Intel 8280 "Cascade Lake" nodes, each with 56 cores. Excellent (close to ideal) weak scaling is observed up to 112,000 MPI ranks.

Strong-scaling experiments on the LUMI supercomputer based at CSC, Finland (LUMI-C, denotes CPU-based hardware and LUMI-G denotes GPU-based hardware) are reported in Figure. 3b. The LUMI system consists of a CPU partition and a GPU partition. In the CPU partition (LUMI-C), each compute node contains two AMD EPYC 7763 processors with 64 cores each, for a total of 128 CPU cores per node. In the GPU partition (LUMI-G), each compute node has one 64-core AMD EPYC "Trento" CPU and four AMD MI250X GPUs. Each MI250X GPU is a multi-chip module composed of two GPU dies (Graphics Compute Dies, GCDs).

Our strong scaling tests are based on a real use case involving a 3D elastostatic model simulating instantaneous deformation, inspired by the 2019 Ridgecrest, California, earthquake sequence (Uphoff et al., 2023). In these experiments, the resources reported on the x-axis are in terms of compute nodes, as CPU experiments used all 128 CPU cores, and GPU experiments used all 8 GPUs. As expected, efficiency decreases as the work (elements/node) decreases due to the cost of communication between the compute nodes, that withstanding the overall time-to-solution is observed to decrease. The solver performance metrics of DOFs/sec/rank and DOFs/sec/GPU are useful to compare the relative gains obtained using either only the CPU, or a mix of CPU-GPU hardware. On LUMI-C, we obtained DOFs/sec/rank in the range of $[1858, 971]$ (smallest to largest node count), whilst on LUMI-G we observed DOFs/sec/GPU in the range of $[20586, 7389]$. When comparing the solver throughput between a single GPU and a single CPU core, we find ratios in the range of $[11, 8]$. For the compute nodes on the LUMI system the ratio of CPU cores to GPUs is $128/8 = 16 > 11$, hence the fastest time-to-solution will be obtained using all CPUs on the compute node.

5 Selected Examples

Recently published `Tandem`-applications span megathrust earthquake cycles on 2D curved geometries (Biemiller et al., 2024), the effect of heterogeneous friction and stress perturbation on 2D strike-slip faulting complexity (Yun et al., 2025b), slow slip

[8] https://github.com/TEAR-ERC/tandem-training

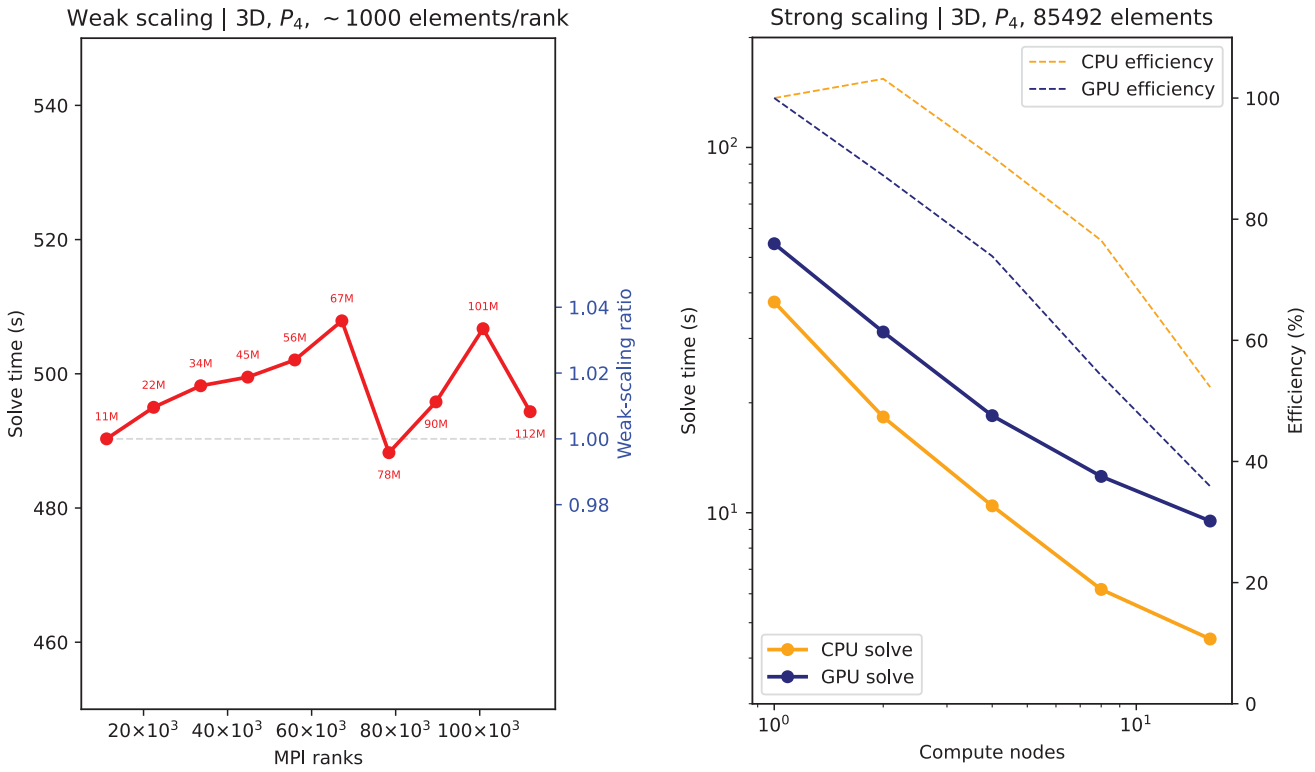

Figure 3. (a) Weak scaling of an elastostatic solve, on Frontera (TACC, USA), using polynomial degree 4 with varying computational mesh sizes (annotated in red, in million elements). The measured time to solution is shown by the red line, and the ideal weak scaling result is shown by the dashed gray line. The right y-axis is the ratio of ideal CPU time over measured CPU time, with ratio values < 1 indicating better than perfect weak scaling and values > 1 indicating sub-optimal weak scaling. (b) Strong scaling of an elastostatic solve on CPUs (LUMI-C, orange lines) and GPUs (LUMI-G, blue lines), using polynomial degree 4 and a small mesh of 85,492 volume elements. This choice allows `Tandem` to run on a limited number of GPUs on LUMI-G, as larger meshes would exceed the memory capacity of the GPUs, while still providing a meaningful strong-scaling challenge.

Alt text: Three alternative kinematic loading prescriptions for a dipping megathrust model, showing which boundaries are fixed, traction-free, or displacement-controlled and the direction of imposed plate-motion vectors. The panels distinguish backslip-style shearing, far-field horizontal shortening, and a case where convergence is accommodated beneath the slab while the overriding plate remains fixed; mesh coarsening illustrates how resolution is concentrated near the fault.

and delayed earthquake triggering on strike-slip faults (Yun et al., 2025a), Cascadia slow slip cycles (Magen et al., 2025), and a theoretical correlation between coseismic and interseismic slip distributions (Oryan and Gabriel, 2025). A detailed exploration of the effect of different state evolution laws (Sec. 2.1) on modeled seismic cycle is also provided in Yun et al. (2025b). In the following, we provide two unpublished, illustrative examples.

5.1 BP7, a 3D volumetric SEAS simulation

`Tandem` participated in the recent "BP7" SEAS community benchmark (Lambert et al., 2023) supported by the Statewide California Earthquake Center (SCEC). The benchmark models a circular velocity-weakening nucleation zone embedded in a 3D, homogeneous, isotropic, elastic whole space. We achieve good agreement with the boundary-integral code BiCyclE (Lapusta et al., 2000; Lapusta and Liu, 2009; Lambert et al., 2025) and the finite-difference code Thrase (Erickson and Dunham, 2014) in this large-scale, long-term SEAS simulations, illustrated in Figs. 4a,b,c. The slight mismatch of the recurrence interval for the aging-law (Figure 4b) is consistent with previous benchmark exercises results and reflects the impact of varying domain size and boundary conditions assumptions in volumetric-based codes and sensitivity to numerical choices (Jiang et al., 2022).

The benchmark setup consists of a planar rate-and-state fault with a velocity-weakening patch surrounded by a velocity-strengthening region (Fig. 4d). The exercises prescribe a smooth stress perturbation in the VW portion of the fault to trigger the first rupture (Figure 4c, d).

To approximate the unbounded whole-space solution with our volumetric code, we embed the 0.8×0.8 km rate-and-state fault in a $2 \times 2 \times 2$ km domain. Constant tectonic loading is imposed via Dirichlet boundaries, with $V_p/2$ prescribed on the outer surfaces at $y = \pm 2$ km and V_p on the central surface ($y = 0$ km), while the remaining faces ($x, z = \pm 2$ km) are treated as traction-free. We use polynomial degree 3 for the DG basis with refined mesh size inside the circular velocity-weakening region and gradual coarsening toward the boundaries to reduce cost. The on-fault element size at the VW portion is 0.03 km, and starting at the VS region and moving towards the boundary, the elements coarsen as $d/2 + 0.03$ km, where d is the distance from the VW circular patch of the fault. This results in 4698 tetrahedral elements, of which 2446 have a face on the fault surface. BP7 consists of four quasi-dynamic scenarios, varying the characteristic slip distance ($D_c = 0.5, 0.53$ mm) and friction law (both aging and slip). We here show results for $D_c = 0.5$ in Fig. 4. One simulation required 81,086 s of wall-clock time on 60 AMD EPYC 7662 processors, corresponding to about 1,350 CPU hours. We compare the evolution of the first earthquake (after the spin-up phase) when using the aging and slip evaluation laws, respectively, in Figure 4e-j. The slip-law solution event grows initially slower (Figure 4e, h) and then outpaces the aging law modeled earthquake (Figure 4f, i) with both solutions fully rupturing the VW patch after 1.8s (Figure 4g, j).

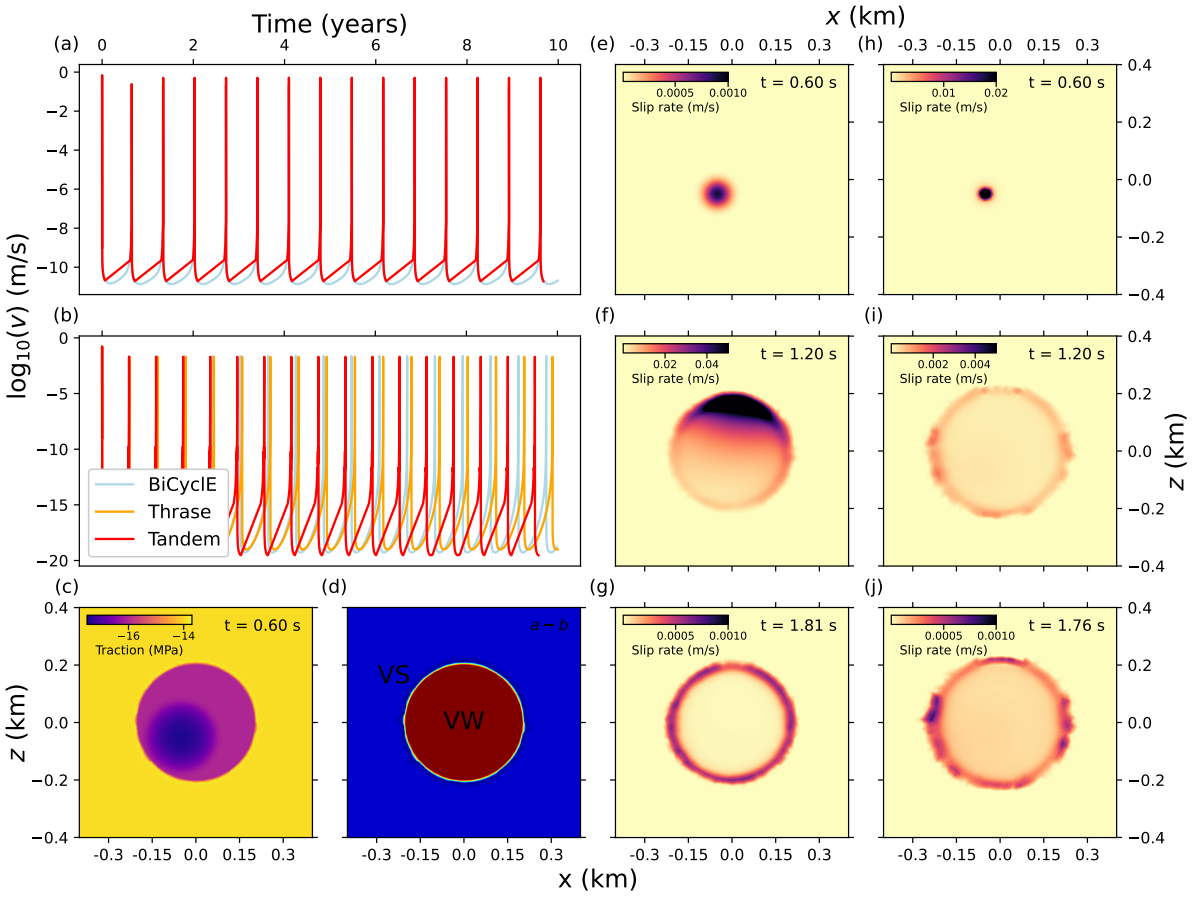

Figure 4. *Tandem* results for the SCEC SEAS benchmark BP7 (Lambert et al., 2023). (a) Temporal evolution of slip rate at the center of the velocity-weakening (VW) patch for the slip law. (b) Same as (a) for the aging law. *Tandem* is compared to the boundary-integral code BiCyclE (Lapusta et al., 2000; Lapusta and Liu, 2009) and the finite-difference code Thrase (Erickson and Dunham, 2014). (c) Shear traction on the fault at $t = 0.6$ s. The first rupture is initiated by a smoothly growing stress perturbation starting at $t = 0$ and $(x, z) = (-0.05, -0.05)$ km. (d) Distribution of $(a - b)$ along the fault, with $(a - b) = \pm 0.006$ in the VW and velocity-strengthening (VS) regions, respectively. (e–g) Propagation of the first rupture for the aging law. (h–j) Same as (e–g) for the slip law. Note the different color scales in each panel.

Alt text: Benchmark comparison demonstrating that Tandem reproduces key BP7 earthquake-cycle characteristics: slip-rate time series align with reference boundary-integral and finite-difference codes; parameter and traction fields define a confined velocity-weakening nucleation region; and rupture snapshots illustrate how the first event initiates from a prescribed perturbation and propagates across the patch, with differing evolution between aging-law and slip-law formulations.

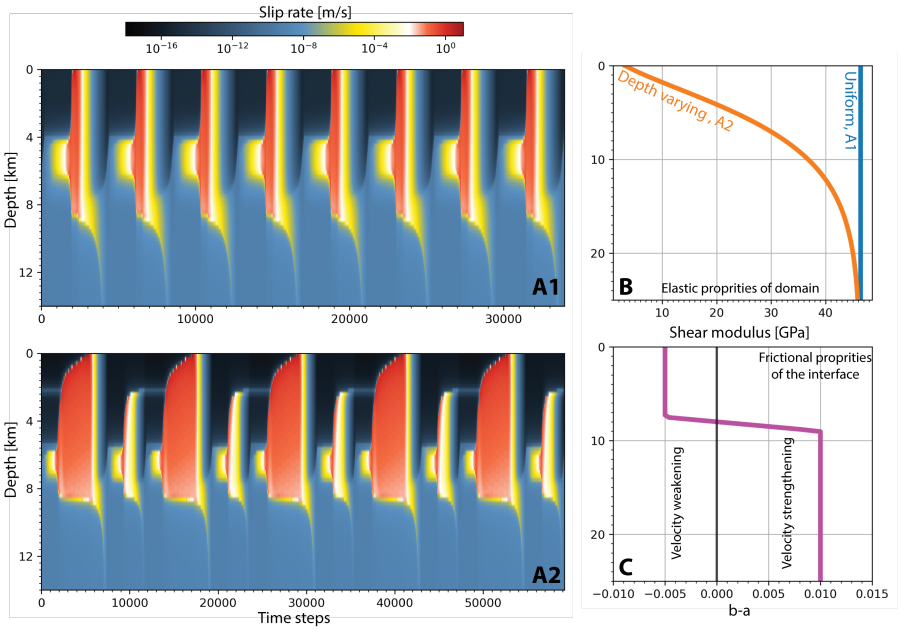

Figure 5. Effects of uniform and depth-varying off-fault elasticity on megathrust earthquake behavior. A – Slip rate along the fault interface for models with uniform (A1) and depth-varying (A2) shear modulus of the domain. B – Shear modulus distribution for the two models. C – Profile of the rate-and-state friction parameter $(b - a)$ used in both models.

Alt text: Sensitivity of modeled megathrust seismic cycling to off-fault rigidity structure: time–depth slip-rate patterns differ between a uniform-rigidity upper plate and one with depth-varying shear modulus, indicating changes in where slip concentrates and how events progress through the cycle. Companion panels provide the depth-dependent shear-modulus profile and the along-interface frictional stability parameter used to isolate the effect of elastic heterogeneity.

5.2 Off-fault megathrust heterogeneity in 2D SEAS simulations.

The elastic structure of the upper plate can play a key role in controlling the behavior of megathrust earthquakes (Prada et al. (2021); Sallarès et al. (2021); Sallarès and Ranero (2019)), yet few numerical quasi-dynamic models explicitly capture this effect. Building upon the BP3 benchmark (Erickson et al., 2023), we design two simple models (Fig. 5) that differ only in their off-fault heterogeneity: one assumes uniform elastic off-fault properties, and the other allows the shear modulus to vary with depth (Fig. 5B), following observational constraints from seismic velocity profiles across global subduction zones (Sallarès and Ranero, 2019). Identical normal stress and frictional properties along the fault interface (Fig. 5C) are used in both models. These example simulations show that even in this simplified setup, earthquake behavior differs markedly between the two scenarios (Fig. 5A). When heterogeneous shear modulus is included, the model produces two distinct types of events, interface-wide ruptures and deeper, confined earthquakes (Fig. 5A2). This difference arises likely because the shallower portion of the

interface, characterized by a lower shear modulus, accumulates stress more slowly and therefore remains unruptured after large events until sufficient stress is rebuilt during subsequent cycles.

6 Perspectives

Physics-based simulations of regional 3D fault systems using Tandem are useful to guide empirical, traditional earthquake rupture forecast models and could be eventually used directly for earthquake hazard and risk estimation (Field et al., 2025). In expensive `Tandem` earthquake-cycle simulations, a limiting factor is the linear solve: hybrid geometric-algebraic multigrid preconditioning with tuned smoothers has been most effective. This approach is algorithmically and memory scalable, i.e., iteration counts are essentially independent of degrees of freedom, with near-ideal weak scaling verified to 112,000 MPI ranks on Frontera (Fig. 3). Currently weak scaling beyond 115k MPI ranks is limited by the graph partitioner ParMETIS, which is not designed for MPI communicators of this large size. Evaluating alternative graph partitioners, and or hierarchical partitioning strategies (e.g. Kong et al. (2018)) should be conducted in future work. More broadly, open, shared implementations, together with community code-comparison benchmarks, accelerate progress and clarify sensitivities. While boundary-integral methods remain faster, volume methods are indispensable for realistic geometries, heterogeneity, and multiphysics, reinforcing our emphasis on robust preconditioners for tractable realistic, volumetric SEAS simulations.

A complementary future opportunity is to reduce the effective cost of these volumetric solves using scientific machine learning methods (e.g., Degen et al., 2023) which are increasingly popular in earthquake modeling, for example, by constructing reduced-order models (ROMs), neural operators or networks (e.g., Rekoske et al., 2023; Zou et al., 2024; Lehmann et al., 2025; Rekoske et al., 2025; Hobson et al., 2025; Liu and Becker, 2025). The discrete Green's function option in `Tandem` already replaces repeated elliptic solves by affine slip–traction maps at the expense of a costly precomputation (Sec. 3.3). Recent ROM studies for SEAS problems show that these maps (Kaveh et al., 2024), and more generally the SEAS dynamics, often evolve on low-dimensional manifolds that can be captured by projection-based surrogates with large speed-ups at controlled error (Magen et al., 2025). Combining SIPG, discrete Green's functions, and ROMs may convert the expensive volumetric stage into a one-time training and compression step, after which many earthquake-cycle simulations, parameter scans, and probabilistic inversions could be run at much lower marginal cost while retaining the geometric flexibility and stability properties of the high-order DG formulation.

7 Conclusions

`Tandem` provides a volumetric, SIPG-based framework for SEAS simulations on unstructured curvilinear meshes that can resolve complex multi-fault geometries, heterogeneous material structure, and various loading conditions in 2D and 3D. The combination of high-order DG discretization, hybrid geometric–algebraic multigrid preconditioning, and performance-portable PETSc/YATeTo kernels yields scalable linear solves on modern CPU and GPU architectures and enables large-scale 3D earthquake-cycle models with near-ideal weak scaling demonstrated to $\sim$112k MPI ranks. The optional discrete Green's function mode offers an alternative approach that trades precomputation and memory for rapid time stepping. The code, documentation, and examples are openly available, including via the Quakeworx Science Gateway in a web browser.

Date & Resources. No data were used in this paper. The `Tandem` software is available at GitHub at https://github.com/TEAR-ERC/tandem. Instructions on how to build and run the code are available at https://tandem.readthedocs.io. Tandem is available via a UTM virtual machine suitable for M1/M2/M3 Mac Users via Zenodo https://doi.org/10.5281/zenodo.12365886] and as "Apps" via the Quakeworx Science gateway at https://quakeworx.org. The input files for both new examples presented in this paper are openly available at Zenodo https://zenodo.org/records/17885293.

Appendix A: Governing Equations

In the following, we adapt the same notation as Uphoff et al. (2023). We denote the physical domain as $\Omega \subset \mathbb{R}^D$ ($D = 2, 3$) with its boundary $\partial\Omega = \Gamma^D \cup \Gamma^N \cup \Gamma^F$ (Dirichlet, Neumann, and internal fault boundaries, respectively). The unknown displacement is $\boldsymbol{u}(\boldsymbol{x}, t)$, the Cauchy stress is $\boldsymbol{\sigma}$, and $\boldsymbol{n}$ denotes the unit normal on Γ^F (pointing from the "$-$" side of the fault to the "$+$" side of the fault). On the exterior boundaries (Γ^D, Γ^N) $\boldsymbol{n}$ is uniquely defined as the outward point unit vector from the exterior boundary.

A1 Linear elasticity in the bulk

In the bulk $\Omega \setminus (\Gamma^F \cup \Gamma^D \cup \Gamma^N)$, we assume small-strain linear elasticity in which the strain and stress is given by

$$\varepsilon_{ij}(\boldsymbol{u}) \;=\; \tfrac{1}{2}\big(u_{i,j} + u_{j,i}\big), \qquad \sigma_{ij}(\boldsymbol{u}) \;=\; c_{ijkl}\,\varepsilon_{kl}(\boldsymbol{u}), \tag{A1}$$

respectively, with an isotropic constitutive tensor $c_{ijkl} = \lambda\,\delta_{ij}\delta_{kl} + \mu(\delta_{ik}\delta_{jl} + \delta_{il}\delta_{jk})$.

We consider two forms of the conservation of linear momentum. The first is the *quasi-static* (QS) regime in which the conservation of momentum is given by

$$-\sigma_{ij,j}(\boldsymbol{u}) \;=\; f_i \qquad \text{in } \Omega \setminus (\Gamma^F \cup \Gamma^D \cup \Gamma^N). \tag{A2}$$

We also consider the *fully dynamic* (FD) regime in which inertia is included in the momentum equation

$$\rho\, \ddot{u}_i - \sigma_{ij,j}(\boldsymbol{u}) \;=\; f_i \qquad \text{in } \Omega \setminus (\Gamma^F \cup \Gamma^D \cup \Gamma^N), \tag{A3}$$

where ρ is the density.

On the exterior boundary of Ω we impose standard Dirichlet and Neumann boundary conditions

$$\boldsymbol{u} = \boldsymbol{g}^D \text{ on } \Gamma^D, \qquad \boldsymbol{\sigma}(\boldsymbol{u})\boldsymbol{n} = \boldsymbol{t}^N \text{ on } \Gamma^N. \tag{A4}$$

A2 Fault kinematics and tractions

Across the fault Γ^F we allow a tangential displacement jump (slip) but no opening,

$$[\![\boldsymbol{u}]\!] \equiv \boldsymbol{u}^+ - \boldsymbol{u}^- \;=\; \boldsymbol{B}\,\boldsymbol{S}, \qquad [\![\boldsymbol{u}]\!] \cdot \boldsymbol{n} \;=\; 0 \quad \text{on } \Gamma^F, \tag{A5}$$

where $\boldsymbol{S}(\boldsymbol{x}, t) \in \mathbb{R}^{D-1}$ is the slip vector, $\boldsymbol{V} = \dot{\boldsymbol{S}}$ is the slip-rate vector, and $\boldsymbol{B} \in \mathbb{R}^{D\times(D-1)}$ collects an orthonormal basis of tangential directions on the fault.

Let $\boldsymbol{t} = \boldsymbol{\sigma}(\boldsymbol{u})\,\boldsymbol{n}$ be the total traction and define the tangential traction components

$$\boldsymbol{T} \;=\; \boldsymbol{B}^T \boldsymbol{t} \in \mathbb{R}^{D-1}, \qquad \sigma_n \;=\; -\boldsymbol{n}^T \boldsymbol{\sigma}(\boldsymbol{u})\,\boldsymbol{n} \;\geq 0 \quad (\text{compression} \geq 0), \tag{A6}$$

where $\boldsymbol{t}$ is the unit vector tangential to Γ^F. If pore pressure p is modeled, we replace σ_n by the *effective* normal stress $\bar{\sigma}_n = \sigma_n - p$.

A3 Rate-and-state friction

Tandem supports both the classic slip-law and aging-law rate-and-state friction (RSF) variations, implemented as a regularized (arcsinh) form (e.g., Rice, 1993; Lapusta et al., 2000). Denoting $V = \|\mathbf{V}\|$, we define the shear strength as

$$\boldsymbol{\tau}_S \;=\; \bar{\sigma}_n \, f(V,\theta) \, \frac{\boldsymbol{V}}{V+\epsilon}, \qquad \epsilon \ll V_0 \text{ (regularization for } V = 0), \tag{A7}$$

with the state variable θ (time dimension), the characteristic slip L, and V_0 being a reference slip rate.

The classical parameterizations of f in rate-and-state friction is the log-formulation, with f given by

$$f(V,\theta) \;=\; f_0 \;+\; a \ln\!\left(\frac{V}{V_0}\right) \;+\; b \ln\!\left(\frac{\theta V_0}{L}\right), \tag{A8}$$

and the state evolution described by either the aging law (Eq. (A9a)), or the slip law (Eq. (A9b)). The latter is given by

$$\dot{\theta} = 1 - \frac{V\theta}{L}, \tag{A9a}$$

$$\dot{\theta} = -\frac{V\theta}{L} \ln\!\left(\frac{V\theta}{L}\right). \tag{A9b}$$

In *Tandem's* implementation we use the *regularized arcsinh formulation* of the state variable which employs a transformed state variable defined as $\psi = f_0 + b \ln\left(\frac{V_0 \theta}{L}\right)$. With this change of variables Eq. (A8) and Eq. (A9a) become

$$f(V,\psi) = a \operatorname{arcsinh}\left(\frac{V}{2V_0} \exp\left(\frac{\psi}{a}\right)\right), \qquad \dot{\psi} = \frac{bV_0}{L}\left(\exp\left(\frac{f_0 - \psi}{b}\right) - \frac{V}{V_0}\right). \tag{A10}$$

The slip law (Eq. (A9b)) can be used with the log-form of f (Eq. (A8)) directly.

A4 Quasi-dynamic radiation damping

To stabilize the QS bulk solve while retaining leading-order inertial effects at the interface, the *radiation-damping* term augments the traction balance (Rice, 1993; Cochard and Madariaga, 1994; Lapusta et al., 2000):

$$-\boldsymbol{T} \;=\; \boldsymbol{\tau}_S \;+\; \eta \boldsymbol{V}, \qquad \eta \;=\; \frac{\mu}{2c_s}, \tag{A11}$$

where c_s is the shear-wave speed and μ the shear modulus (so η is half the shear impedance in anti-plane; the same scalar η is applied to each tangential component). The addition of the radiation damping term, when used in conjunction with the QS momentum equation is referred to as a *quasi-dynamic* (QD) SEAS model. The coupled QD SEAS system then is

$$-\sigma_{ij,j}(\boldsymbol{u}) = f_i \qquad \text{in } \Omega \setminus \Gamma^F, \tag{A12}$$

$$[\![\boldsymbol{u}]\!] = \boldsymbol{B}\,\boldsymbol{S}, \quad [\![\boldsymbol{u}]\!]\cdot\boldsymbol{n} = 0 \qquad \text{on } \Gamma^F, \tag{A13}$$

$$-\boldsymbol{T} = \bar{\sigma}_n\, f(V,\theta)\,\frac{\boldsymbol{V}}{V+\epsilon} + \eta\,\boldsymbol{V} \qquad \text{on } \Gamma^F, \tag{A14}$$

$$\dot{\boldsymbol{S}} = \boldsymbol{V}, \qquad \dot{\theta} = \begin{cases} 1 - \dfrac{V\theta}{L}, & \text{(aging)} \\ -\dfrac{V\theta}{L}\ln\left(\dfrac{V\theta}{L}\right), & \text{(slip)} \end{cases} \qquad \text{on } \Gamma^F, \tag{A15}$$

with $\boldsymbol{T} = \boldsymbol{B}^T\boldsymbol{\sigma}(\boldsymbol{u})\boldsymbol{n}$ and $\bar{\sigma}_n$ from Eq. (A6).

A5 Initial and boundary data.

Provide $\boldsymbol{u}(\cdot,0)$ (or static equilibrium), $\boldsymbol{S}(\cdot,0)$, $\theta(\cdot,0)$ on Γ^F, and loading data $(\boldsymbol{g}^D, \boldsymbol{t}^N)$ on (Γ^D, Γ^N). If fluids are included, replace σ_n by $\bar{\sigma}_n = \sigma_n - p(\boldsymbol{x},t)$ with p from a (possibly 1D/2D) diffusion model; all interface equations above remain unchanged.

Author contributions. Conceptualization: AAG; Data curation: AAG, PK, BO, TU, JY, DAM; Formal analysis: YM, BO, DAM; Funding acquisition: AAG, BO, DAM; Investigation: YM, BO, JY; Methodology: AAG, YM, BO, JY, DAM; Project administration: AAG, DAM; Resources: AAG, DAM; Software: PK, YM, TU, JY, DAM; Supervision: AAG, DAM; Validation: AAG, DAM; Visualization: AAG, YM, BO, TU, JY, DAM; Writing – original draft: AAG; Writing – review & editing: PK, YM, BO, TU, JY, DAM

Competing interests. All authors declare no competing interests.

Acknowledgements. We thank Valere Lambert, Brittany Erickson and Junle Jiang for leading the BP7 SEAS community benchmark exercise, and Valere and Brittany for making their BP7 results available for use in this publication. This project was supported by NSF (grants no. EAR-2143413, EAR-2121568, OAC-2139536, OAC-2311208), Horizon Europe (Geo-INQUIRE, project no. 101058518 and ChEESE-2P, 101058129), NASA (grant no. 80NSSC20K0495), the Statewide California Earthquake Center (SCEC award 25341) and Schmidt Science, LLC. We acknowledge financial support from the Cecil H. and Ida M. Green's Foundation for Earth Sciences for two Tandem Hackathons that advanced the development of the Tandem code. We gratefully acknowledge the Texas Advanced Computing Center (TACC), and the Gauss Centre for Supercomputing (LRZ, project pn49ha). Additional computing resources were provided by the Institute of Geophysics of LMU Munich Oeser et al. (2006).

References

Aagaard, B. T., Knepley, M. G., and Williams, C. A.: A domain decomposition approach to implementing fault slip in finite-element models of quasi-static and dynamic crustal deformation, Journal of Geophysical Research: Solid Earth, 118, 3059–3079, https://doi.org/https://doi.org/10.1002/jgrb.50217, 2013.

Abdelmeguid, M. and Elbanna, A.: Modeling Sequences of Earthquakes and Aseismic Slip (SEAS) in Elasto-Plastic Fault Zones With a Hybrid Finite Element Spectral Boundary Integral Scheme, Journal of Geophysical Research: Solid Earth, 127, e2022JB024 548, https://doi.org/https://doi.org/10.1029/2022JB024548, e2022JB024548 2022JB024548, 2022.

Abhyankar, S., Brown, J., Constantinescu, E., Ghosh, D., and Smith, B. F.: PETSc/TS: A modern scalable DAE/ODE solver library, Preprint ANL/MCS-P5061-0114, Argonne National Laboratory, 2014.

Allison, K. L. and Dunham, E. M.: Earthquake cycle simulations with rate-and-state friction and power-law viscoelasticity, Tectonophysics, 733, 232–256, https://doi.org/https://doi.org/10.1016/j.tecto.2017.10.021, 2018.

Almquist, M. and Dunham, E. M.: Elastic wave propagation in anisotropic solids using energy-stable finite differences with weakly enforced boundary and interface conditions, Journal of Computational Physics, 424, 109 842, https://doi.org/10.1016/j.jcp.2020.109842, 2021.

Amestoy, P. R., Duff, I. S., L'Excellent, J.-Y., and Koster, J.: A fully asynchronous multifrontal solver using distributed dynamic scheduling, SIAM Journal on Matrix Analysis and Applications, 23, 15–41, 2001.

Amestoy, P. R., Guermouche, A., L'Excellent, J.-Y., and Pralet, S.: Hybrid scheduling for the parallel solution of linear systems, Parallel Computing, 32, 136–156, 2006.

Arnold, D. N., Brezzi, F., Cockburn, B., and Marini, L. D.: Unified Analysis of Discontinuous Galerkin Methods for Elliptic Problems, Journal on Numerical Analysis, 39, 1749–1779, https://doi.org/10.1137/S0036142901384162, 2002.

Balay, S., Gropp, W. D., McInnes, L. C., and Smith, B. F.: Efficient Management of Parallelism in Object Oriented Numerical Software Libraries, in: Modern Software Tools in Scientific Computing, edited by Arge, E., Bruaset, A. M., and Langtangen, H. P., pp. 163–202, Birkhäuser Press, 1997.

Balay, S., Abhyankar, S., Adams, M. F., Brown, J., Brune, P., Buschelman, K., Dalcin, L., Eijkhout, V., Gropp, W. D., Kaushik, D., Knepley, M. G., McInnes, L. C., Rupp, K., Smith, B. F., Zampini, S., and Zhang, H.: PETSc Web page, http://www.mcs.anl.gov/petsc, http://www.mcs.anl.gov/petsc, 2015.

Balay, S., Abhyankar, S., Adams, M. F., Brown, J., Brune, P., Buschelman, K., Dalcin, L., Dener, A., Eijkhout, V., Gropp, W. D., Karpeyev, D., Kaushik, D., Knepley, M. G., May, D. A., McInnes, L. C., Mills, R. T., Munson, T., Rupp, K., Sanan, P., Smith, B. F., Zampini, S., Zhang, H., and Zhang, H.: PETSc Users Manual, Tech. Rep. ANL-95/11 - Revision 3.15, Argonne National Laboratory, https://www.mcs.anl.gov/petsc, 2021.

Barbot, S.: Slow-slip, slow earthquakes, period-two cycles, full and partial ruptures, and deterministic chaos in a single asperity fault, Tectonophysics, 768, 228 171, https://doi.org/https://doi.org/10.1016/j.tecto.2019.228171, 2019.

Barbot, S., Lapusta, N., and Avouac, J.-P.: Under the Hood of the Earthquake Machine: Toward Predictive Modeling of the Seismic Cycle, Science, 336, 707–710, https://doi.org/10.1126/science.1218796, 2012.

Barker, M., Olabarriaga, S. D., Wilkins-Diehr, N., Gesing, S., Katz, D. S., Shahand, S., Henwood, S., Glatard, T., Jeffery, K., Corrie, B., et al.: The global impact of science gateways, virtual research environments and virtual laboratories, Future Generation Computer Systems, 95, 240–248, 2019.

Biemiller, J., Gabriel, A.-A., May, D., and Staisch, L.: Subduction zone geometry modulates the megathrust earthquake cycle: magnitude, recurrence, and variability, Journal of Geophysical Research: Solid Earth, 129, e2024JB029 191, 2024.

Börm, S., Grasedyck, L., and Hackbusch, W.: Introduction to hierarchical matrices with applications, Engineering analysis with boundary elements, 27, 405–422, 2003.

Bradley, A. M.: Software for Efficient Static Dislocation–Traction Calculations in Fault Simulators, Seismological Research Letters, 85, 1358–1365, https://doi.org/10.1785/0220140092, 2014.

Bürgmann, R.: The geophysics, geology and mechanics of slow fault slip, Earth and Planetary Science Letters, 495, 112–134, https://doi.org/https://doi.org/10.1016/j.epsl.2018.04.062, 2018.

Chapple, W. M. and Tullis, T. E.: Evaluation of the forces that drive the plates, Journal of Geophysical Research (1896-1977), 82, 1967–1984, https://doi.org/https://doi.org/10.1029/JB082i014p01967, 1977.

Chen, A., Erickson, B. A., Kozdon, J. E., and Choi, J.: Matrix-free SBP-SAT finite difference methods and the multigrid preconditioner on GPUs, in: Proceedings of the 38th ACM International Conference on Supercomputing, pp. 400–412, 2024.

Cheng, J., Bhat, H. S., Almakari, M., Lecampion, B., and Peruzzo, C.: FASTDASH: An Implementation of 3D Earthquake Cycle Simulation on Complex Fault Systems Using the Boundary Element Method Accelerated by H-matrices, Geophysical Journal International, p. ggaf230, 2025.

Chourasia, A., Youn, C., Silva, F., Olsen, B., Zhao, C., Yun, J., Maechling, P. J., May, D. A., Elbanna, A. E., Gabriel, A.-A., and Ben-Zion, Y.: Quakeworx science gateway: A custom instance of OneSciencePlace, https://doi.org/10.5281/zenodo.13864099, 2024.

Cochard, A. and Madariaga, R.: Dynamic faulting under rate-dependent friction, Pure and Applied Geophysics, 142, 419–445, 1994.

Day, S. M., Dalguer, L. A., Lapusta, N., and Liu, Y.: Comparison of finite difference and boundary integral solutions to three-dimensional spontaneous rupture, Journal of Geophysical Research: Solid Earth, 110, 2005.

Degen, D., Caviedes Voullième, D., Buiter, S., Hendricks Franssen, H.-J., Vereecken, H., González-Nicolás, A., and Wellmann, F.: Perspectives of physics-based machine learning strategies for geoscientific applications governed by partial differential equations, Geoscientific Model Development, 16, 7375–7409, 2023.

Denolle, M. A., Tape, C., Bozdağ, E., Wang, Y., Waldhauser, F., Gabriel, A., Braunmiller, J., Chow, B., Ding, L., Feng, K., Ghosh, A., Groebner, N., Gupta, A., Krauss, Z., McPherson, A. M., Nagaso, M., Niu, Z., Ni, Y., Örsvuran, R., Pavlis, G., Rodriguez-Cardozo, F., Sawi, T., Schaff, D., Schliwa, N., Schneller, D., Shi, Q., Thurin, J., Wang, C., Wang, K., Wong, J. W. C., Wolf, S., and Yuan, C.: Training

the Next Generation of Seismologists: Delivering Research-Grade Software Education for Cloud and HPC Computing Through Diverse Training Modalities, Seismological Research Letters, 96, 3265–3279, https://doi.org/10.1785/0220240413, 2025.

Dieterich, J. H.: Modeling of rock friction: 1. Experimental results and constitutive equations, Journal of Geophysical Research: Solid Earth, 84, 2161–2168, https://doi.org/https://doi.org/10.1029/JB084iB05p02161, 1979.

Dieterich, J. H. and Kilgore, B. D.: Direct observation of frictional contacts: New insights for state-dependent properties, Pure and Applied Geophysics, 143, 283–302, https://doi.org/10.1007/BF00874332, 1994.

Eberhart-Phillips, D., Bannister, S., Reyners, M., and Henrys, S.: New Zealand Wide model 2.2 seismic velocity and Qs and Qp models for New Zealand, https://doi.org/10.5281/zenodo.3779523, 2020.

Erickson, B. A. and Dunham, E. M.: An efficient numerical method for earthquake cycles in heterogeneous media: Alternating sub-basin and surface-rupturing events on faults crossing a sedimentary basin, Journal of Geophysical Research: Solid Earth, 119, 3290–3316, https://doi.org/https://doi.org/10.1002/2013JB010614, 2014.

Erickson, B. A., Dunham, E. M., and Khosravifar, A.: A finite difference method for off-fault plasticity throughout the earthquake cycle, Journal of the Mechanics and Physics of Solids, 109, 50–77, 2017.

Erickson, B. A., Jiang, J., Barall, M., Lapusta, N., Dunham, E. M., Harris, R., Abrahams, L. S., Allison, K. L., Ampuero, J.-P., Barbot, S., and C., C.: The community code verification exercise for simulating sequences of earthquakes and aseismic slip (SEAS), Seismological Research Letters, 91, 874–890, 2020.

Erickson, B. A., Jiang, J., Lambert, V., Barbot, S. D., Abdelmeguid, M., Almquist, M., Ampuero, J.-P., Ando, R., Cattania, C., Chen, A., et al.: Incorporating full elastodynamic effects and dipping fault geometries in community code verification exercises for simulations of earthquake sequences and aseismic slip (SEAS), Bulletin of the Seismological Society of America, 113, 499–523, 2023.

Fehn, N., Munch, P., Wall, W. A., and Kronbichler, M.: Hybrid multigrid methods for high-order discontinuous Galerkin discretizations, Journal of Computational Physics, 415, 109 538, 2020.

Field, E. H., Hatem, A. E., Shaw, B. E., Page, M. T., Mai, P. M., Milner, K. R., Llenos, A. L., Michael, A. J., Pollitz, F. F., Thompson Jobe, J., Parsons, T., Zielke, O., Shelly, D. R., Gabriel, A., McPhillips, D., Briggs, R. W., Cochran, E. S., Luco, N., Petersen, M. D., Powers, P. M., Rubinstein, J. L., Shumway, A. M., van der Elst, N. J., Zeng, Y., Duross, C. B., and Altekruse, J. M.: A Scientific Vision and Roadmap for Earthquake Rupture Forecast Developments, A USGS Perspective, Bulletin of the Seismological Society of America, 115, 2523–2552, https://doi.org/10.1785/0120240217, 2025.

Forsyth, D. and Uyeda, S.: On the relative importance of the driving forces of plate motion, Geophysical Journal International, 43, 163–200, 1975.

Gabriel, A.-A., Li, D., Chiocchetti, S., Tavelli, M., Peshkov, I., Romenski, E., and Dumbser, M.: A unified first-order hyperbolic model for nonlinear dynamic rupture processes in diffuse fracture zones, Philosophical Transactions of the Royal Society A, 379, 20200 130, 2021.

Gabriel, A.-A., Garagash, D. I., Palgunadi, K. H., and Mai, P. M.: Fault size–dependent fracture energy explains multiscale seismicity and cascading earthquakes, Science, 385, eadj9587, 2024.

Gabriel, A.-A., Kurapati, V., Niu, Z., Schliwa, N., Schneller, D., Ulrich, T., Dorozhinskii, R., Krenz, L., Uphoff, C., Wolf, S., Breuer, A., Heinecke, A., Pelties, C., Rettenberger, S., Wollherr, S., and Bader, M.: SeisSol, https://doi.org/10.5281/zenodo.15685917, 2025.

Geuzaine, C. and Remacle, J.-F.: Gmsh: A 3-D finite element mesh generator with built-in pre- and post-processing facilities, International Journal for Numerical Methods in Engineering, 79, 1309–1331, https://doi.org/https://doi.org/10.1002/nme.2579, 2009.

Harvey, T. W., Erickson, B. A., and Kozdon, J. E.: A High-Order Accurate Summation-By-Parts Finite Difference Method for Fully-Dynamic Earthquake Sequence Simulations Within Sedimentary Basins, Journal of Geophysical Research: Solid Earth, 128, e2022JB025 357, https://doi.org/https://doi.org/10.1029/2022JB025357, e2022JB025357 2022JB025357, 2023.

Heinecke, A., Breuer, A., Rettenberger, S., Bader, M., Gabriel, A.-A., Pelties, C., Bode, A., Barth, W., Liao, X.-K., Vaidyanathan, K., et al.: Petascale high-order dynamic rupture earthquake simulations on heterogeneous supercomputers, in: SC'14: Proceedings of the International Conference for High Performance Computing, Networking, Storage and Analysis, pp. 3–14, IEEE, 2014.

Helmstetter, A. and Shaw, B. E.: Afterslip and aftershocks in the rate-and-state friction law, Journal of Geophysical Research: Solid Earth, 114, https://doi.org/https://doi.org/10.1029/2007JB005077, 2009.

Herrera, M. T., Crempien, J. G., Cembrano, J., and Moreno, M.: Seismic cycle controlled by subduction geometry: novel 3-D quasi-dynamic model of Central Chile megathrust, Geophysical Journal International, 237, 772–787, 2024.

Hesthaven, J. S. and Warburton, T.: Nodal Discontinuous Galerkin Methods, Springer, New York, USA, ISBN 978-0-387-72065-4, https://doi.org/10.1007/978-0-387-72067-8, 2008.

Hobson, G. M., May, D. A., and Gabriel, A.-A.: Quantifying the Influence of Fault Geometry via Mesh Morphing With Applications to Earthquake Dynamic Rupture and Thermal Models of Subduction, Geochemistry, Geophysics, Geosystems, 26, e2025GC012 531, https://doi.org/https://doi.org/10.1029/2025GC012531, 2025.

Ierusalimschy, R., de Figueiredo, L. H., and Filho, W. C.: Lua — An Extensible Extension Language, Software: Practice and Experience, 26, 635–652, https://doi.org/https://doi.org/10.1002/(SICI)1097-024X(199606)26:6<635::AID-SPE26>3.0.CO;2-P, 1996.

Igel, H.: Computational seismology: a practical introduction, Oxford University Press, 2017.

Jiang, J., Erickson, B. A., Lambert, V. R., Ampuero, J.-P., Ando, R., Barbot, S. D., Cattania, C., Zilio, L. D., Duan, B., Dunham, E. M., Gabriel, A.-A., Lapusta, N., Li, D., Li, M., Liu, D., Liu, Y., Ozawa, S., Pranger, C., and van Dinther, Y.: Community-Driven Code Comparisons for Three-Dimensional Dynamic Modeling of Sequences of Earthquakes and Aseismic Slip, Journal of Geophysical Research: Solid Earth, 127, e2021JB023 519, https://doi.org/https://doi.org/10.1029/2021JB023519, 2022.

Kaneko, Y., Ampuero, J.-P., and Lapusta, N.: Spectral-element simulations of long-term fault slip: Effect of low-rigidity layers on earthquake-cycle dynamics, Journal of Geophysical Research: Solid Earth, 116, https://doi.org/https://doi.org/10.1029/2011JB008395, 2011.

Karypis, G. and Kumar, V.: A fast and high quality multilevel scheme for partitioning irregular graphs, Journal on Scientific Computing, 20, 359–392, 1998.

Kato, N.: Seismic cycle on a strike-slip fault with rate-and state-dependent strength in an elastic layer overlying a viscoelastic half-space, Earth, Planets and Space, 54, 1077–1083, 2002.

Kaveh, H., Avouac, J. P., and Stuart, A. M.: Spatiotemporal forecast of extreme events in a chaotic model of slow slip events, Geophysical Journal International, 240, 870–885, https://doi.org/10.1093/gji/ggae417, 2024.

Kirby, R. M., Sherwin, S. J., and Cockburn, B.: To CG or to HDG: a comparative study, Journal of Scientific Computing, 51, 183–212, 2012.

Kong, F., Stogner, R. H., Gaston, D. R., Peterson, J. W., Permann, C. J., Slaughter, A. E., and Martineau, R. C.: A general-purpose hierarchical mesh partitioning method with node balancing strategies for large-scale numerical simulations, in: 2018 IEEE/ACM 9th workshop on latest advances in scalable algorithms for large-scale systems (ScalA), pp. 65–72, IEEE, 2018.

Krenz, L., Uphoff, C., Ulrich, T., Gabriel, A.-A., Abrahams, L. S., Dunham, E. M., and Bader, M.: 3D Acoustic-Elastic Coupling with Gravity: The Dynamics of the 2018 Palu, Sulawesi Earthquake and Tsunami, in: Proceedings of the International Conference for High Performance Computing, Networking, Storage and Analysis, SC '21, Association for Computing Machinery, New York, NY, USA, ISBN 9781450384421, https://doi.org/10.1145/3458817.3476173, 2021.

Krenz, L., Wolf, S., Hillers, G., Gabriel, A., and Bader, M.: Numerical Simulations of Seismoacoustic Nuisance Patterns from an Induced M 1.8 Earthquake in the Helsinki, Southern Finland, Metropolitan Area, Bulletin of the Seismological Society of America, 113, 1596–1615, https://doi.org/10.1785/0120220225, 2023.

Lambert, V. and Barbot, S.: Contribution of viscoelastic flow in earthquake cycles within the lithosphere-asthenosphere system, Geophysical Research Letters, 43, 10,142–10,154, https://doi.org/https://doi.org/10.1002/2016GL070345, 2016.

Lambert, V. and Lapusta, N.: Resolving Simulated Sequences of Earthquakes and Fault Interactions: Implications for Physics-Based Seismic Hazard Assessment, Journal of Geophysical Research: Solid Earth, 126, e2021JB022 193, https://doi.org/https://doi.org/10.1029/2021JB022193, e2021JB022193 2021JB022193, 2021.

Lambert, V., Jiang, J., and Erickson, B. A.: SEAS Benchmark Problems BP7-QD/FD-A/S, https://scecdata.usc.edu/cvws/seas/download/SEAS_BP7_May2023rev.pdf, SEAS community benchmark description, 2023.

Lambert, V. R., Erickson, B. A., Jiang, J., Dunham, E. M., Kim, T., Ampuero, J.-P., Ando, R., Cappa, F., Dublanchet, P., Elbanna, A., et al.: Community-driven code comparisons for simulations of fluid-induced aseismic slip, Journal of Geophysical Research: Solid Earth, 130, e2024JB030 601, 2025.

Lapusta, N. and Liu, Y.: Three-dimensional boundary integral modeling of spontaneous earthquake sequences and aseismic slip, Journal of Geophysical Research: Solid Earth, 114, https://doi.org/https://doi.org/10.1029/2008JB005934, 2009.

Lapusta, N., Rice, J. R., Ben-Zion, Y., and Zheng, G.: Elastodynamic analysis for slow tectonic loading with spontaneous rupture episodes on faults with rate- and state-dependent friction, Journal of Geophysical Research: Solid Earth, 105, 23 765–23 789, https://doi.org/https://doi.org/10.1029/2000JB900250, 2000.

Lavier, L. L., Tong, X., and Biemiller, J.: The mechanics of creep, slow slip events, and earthquakes in mixed brittle-ductile fault zones, Journal of Geophysical Research: Solid Earth, 126, e2020JB020 325, 2021.

Lehmann, F., Gatti, F., and Clouteau, D.: Multiple-input Fourier Neural Operator (MIFNO) for source-dependent 3D elastodynamics, Journal of Computational Physics, 527, 113 813, https://doi.org/https://doi.org/10.1016/j.jcp.2025.113813, 2025.

Li, D. and Liu, Y.: Spatiotemporal evolution of slow slip events in a nonplanar fault model for northern Cascadia subduction zone, Journal of Geophysical Research: Solid Earth, 121, 6828–6845, https://doi.org/https://doi.org/10.1002/2016JB012857, 2016.

Liu, D. and Becker, T. W.: Earthquake rupture dynamics from graph neural networks, Journal of Geophysical Research: Solid Earth, 130, e2025JB031 981, 2025.

Liu, D., Duan, B., and Luo, B.: EQsimu: a 3-D finite element dynamic earthquake simulator for multicycle dynamics of geometrically complex faults governed by rate-and state-dependent friction, Geophysical Journal International, 220, 598–609, 2020.

Liu, Y. and Rice, J. R.: Aseismic slip transients emerge spontaneously in three-dimensional rate and state modeling of subduction earthquake sequences, Journal of Geophysical Research: Solid Earth, 110, https://doi.org/https://doi.org/10.1029/2004JB003424, 2005.

Luo, B., Duan, B., and Liu, D.: 3D Finite-Element Modeling of Dynamic Rupture and Aseismic Slip over Earthquake Cycles on Geometrically Complex Faults, Bulletin of the Seismological Society of America, 110, 2619–2637, https://doi.org/10.1785/0120200047, 2020.

Ma, X., Hajarolasvadi, S., Albertini, G., Kammer, D. S., and Elbanna, A. E.: A hybrid finite element-spectral boundary integral approach: Applications to dynamic rupture modeling in unbounded domains, International Journal for Numerical and Analytical Methods in Geomechanics, 43, 317–338, https://doi.org/10.1002/nag.2865, 2019.

Magen, Y., May, D., and Gabriel, A.-A.: Reduced-order modelling of Cascadia's slow slip cycles, EarthArXiv, https://doi.org/10.31223/X5QT7V, 2025.

Mallick, R., Lambert, V., and Meade, B.: On the Choice and Implications of Rheologies That Maintain Kinematic and Dynamic Consistency Over the Entire Earthquake Cycle, Journal of Geophysical Research: Solid Earth, 127, e2022JB024 683, https://doi.org/https://doi.org/10.1029/2022JB024683, e2022JB024683 2022JB024683, 2022.

May, D. A., Brown, J., and Le Pourhiet, L.: A scalable, matrix-free multigrid preconditioner for finite element discretizations of heterogeneous Stokes flow, Computer Methods in Applied Mechanics and Engineering, 290, 496–523, 2015.

Mckay, M. B., Erickson, B. A., and Kozdon, J. E.: A computational method for earthquake cycles within anisotropic media, Geophysical Journal International, 219, 816–833, https://doi.org/10.1093/gji/ggz320, 2019.

Meade, B. J.: Kinematic afterslip patterns, Geophysical Research Letters, 51, e2023GL105 797, 2024.

Mercerat, E. D. and Glinsky, N.: A nodal high-order discontinuous Galerkin method for elastic wave propagation in arbitrary heterogeneous media, Geophysical Journal International, 201, 1101–1118, 2015.

Mia, M. S., Abdelmeguid, M., and Elbanna, A. E.: Spatio-temporal clustering of seismicity enabled by off-fault plasticity, Geophys. Res. Lett., 49, https://doi.org/10.1029/2021GL097601, 2022.

Moczo, P., Kristek, J., Gabriel, A.-A., Chaljub, E., Ampuero, J.-P., Sanchez-Sesma, F., Galis, M., Gregor, D., and Kristekova, M.: Numerical wave propagation simulation, in: The 6th IASPEI/IAEE International Symposium: Effects of Surface Geology on Seismic Motion, http://www.nuquake.eu/Publications/Moczo_etal_ESG2021.pdf, 2021.

Obara, K. and Kato, A.: Connecting slow earthquakes to huge earthquakes, Science, 353, 253–257, https://doi.org/10.1126/science.aaf1512, 2016.

Oeser, J., Bunge, H.-P., and Mohr, M.: Cluster design in the earth sciences tethys, in: International conference on high performance computing and communications, pp. 31–40, Springer, 2006.

Oryan, B.: Tandem Image for UTM Virtual Machine Suitable for M1/M2/M3 Mac Users, https://doi.org/10.5281/zenodo.12365886, 2024.

Oryan, B. and Gabriel, A.-A.: Do Coupled Megathrusts Rupture?, EarthArXiv, https://doi.org/10.31223/X5HB3N, 2025.

Ozawa, S., Ida, A., Hoshino, T., and Ando, R.: Large-scale earthquake sequence simulations on 3-D non-planar faults using the boundary element method accelerated by lattice H-matrices, Geophysical Journal International, 232, 1471–1481, 2023.

Pelties, C., De la Puente, J., Ampuero, J.-P., Brietzke, G. B., and Käser, M.: Three-dimensional dynamic rupture simulation with a high-order discontinuous Galerkin method on unstructured tetrahedral meshes, Journal of Geophysical Research: Solid Earth, 117, 2012.

Perez-Silva, A., Kaneko, Y., Savage, M., Wallace, L., and Warren-Smith, E.: Characteristics of Slow Slip Events Explained by Rate-Strengthening Faults Subject to Periodic Pore Fluid Pressure Changes, Journal of Geophysical Research: Solid Earth, 128, e2022JB026 332, https://doi.org/https://doi.org/10.1029/2022JB026332, 2023.

Prada, M., Galvez, P., Ampuero, J.-P., Sallarès, V., Sánchez-Linares, C., Macías, J., and Peter, D.: The Influence of Depth-Varying Elastic Properties of the Upper Plate on Megathrust Earthquake Rupture Dynamics and Tsunamigenesis, Journal of Geophysical Research: Solid Earth, 126, e2021JB022 328, https://doi.org/10.1029/2021JB022328, 2021.

Prescott-Werner, T. and TOML Community: TOML: Tom's Obvious, Minimal Language, https://github.com/toml-lang/toml, version 1.0.0 specification and documentation. Accessed: 2025-12-10.

Reinarz, A., Charrier, D. E., Bader, M., Bovard, L., Dumbser, M., K. Duru, F. F., Gabriel, A.-A., Gallard, J.-M., Köppel, S., Krenz, L., Rannabauer, L., Rezzolla, L., Samfass, P., Tavelli, M., and Weinzierl, T.: ExaHyPE: An engine for parallel dynamically adaptive simulations of wave problems, Computational Physics Communications, p. 107251, 2020.

Rekoske, J. M., Gabriel, A.-A., and May, D. A.: Instantaneous Physics-Based Ground Motion Maps Using Reduced-Order Modeling, Journal of Geophysical Research: Solid Earth, 128, 2023.

Rekoske, J. M., May, D. A., and Gabriel, A.-A.: Reduced-order modelling for complex three-dimensional seismic wave propagation, Geophysical Journal International, 241, 526–548, https://doi.org/10.1093/gji/ggaf049, 2025.

Rice, J. R.: Spatio-temporal complexity of slip on a fault, Journal of Geophysical Research: Solid Earth, 98, 9885–9907, https://doi.org/https://doi.org/10.1029/93JB00191, 1993.

Rice, J. R. and Tse, S. T.: Dynamic motion of a single degree of freedom system following a rate and state dependent friction law, Journal of Geophysical Research: Solid Earth, 91, 521–530, 1986.

Rivière, B.: Discontinuous Galerkin Methods for Solving Elliptic and Parabolic Equations, Society for Industrial and Applied Mathematics, ISBN 978-0-898716-56-6, https://doi.org/10.1137/1.9780898717440, 2008.

Romanet, P. and Ozawa, S.: Fully dynamic earthquake cycle simulations on a nonplanar fault using the spectral boundary integral element method (sBIEM), Bulletin of the Seismological Society of America, 112, 78–97, 2022.

Romanet, P., Ampuero, J.-P., Cappa, F., Scuderi, M. M., and Chaillat, S.: Combined boundary element and finite volume methods for modelling fluid-induced seismicity in fault networks within low-permeability rocks, Geophysical Journal International, 243, ggaf377, https://doi.org/10.1093/gji/ggaf377, 2025.

Rønquist, E. M. and Patera, A. T.: Spectral element multigrid. I. Formulation and numerical results, Journal of Scientific Computing, 2, 389–406, 1987.

Rudi, J., Malossi, A. C. I., Isaac, T., Stadler, G., Gurnis, M., Staar, P. W. J., Ineichen, Y., Bekas, C., Curioni, A., and Ghattas, O.: An extreme-scale implicit solver for complex PDEs: highly heterogeneous flow in earth's mantle, in: Proceedings of the International Conference for High Performance Computing, Networking, Storage and Analysis, SC '15, Association for Computing Machinery, New York, NY, USA, ISBN 9781450337236, https://doi.org/10.1145/2807591.2807675, 2015.

Ruina, A.: Slip instability and state variable friction laws, Journal of Geophysical Research: Solid Earth, 88, 10 359–10 370, https://doi.org/https://doi.org/10.1029/JB088iB12p10359, 1983.

Sallarès, V. and Ranero, C. R.: Upper-plate rigidity determines depth-varying rupture behaviour of megathrust earthquakes, Nature, 576, 96–101, 2019.

Sallarès, V., Prada, M., Riquelme, S., Meléndez, A., Calahorrano, A., Grevemeyer, I., and Ranero, C. R.: Large slip, long duration, and moderate shaking of the Nicaragua 1992 tsunami earthquake caused by low near-trench rock rigidity, Science Advances, 7, eabg8659, 2021.

Savage, J. C.: A dislocation model of strain accumulation and release at a subduction zone, Journal of Geophysical Research: Solid Earth, 88, 4984–4996, 1983.

Schroeder, W., Martin, K. M., and Lorensen, W. E.: The visualization toolkit (2nd ed.): an object-oriented approach to 3D graphics, Prentice-Hall, Inc., USA, ISBN 0139546944, 1998.

Segall, P. and Bradley, A. M.: Slow-slip evolves into megathrust earthquakes in 2D numerical simulations, Geophysical Research Letters, 39, https://doi.org/https://doi.org/10.1029/2012GL052811, 2012.

Shi, P., Wei, M., and Barbot, S.: Contribution of Viscoelastic Stress to the Synchronization of Earthquake Cycles on Oceanic Transform Faults, Journal of Geophysical Research: Solid Earth, 127, e2022JB024 069, https://doi.org/https://doi.org/10.1029/2022JB024069, e2022JB024069 2022JB024069, 2022.

Sun, X. and Zhang, Z.: A new finite-difference method for earthquake cycles accelerated by GPU and multigrid method, Geophysical Journal International, 241, 1029–1041, https://doi.org/10.1093/gji/ggaf085, 2025.

Tago, J., Cruz-Atienza, V. M., Virieux, J., Etienne, V., and Sánchez-Sesma, F. J.: A 3D hp-adaptive discontinuous Galerkin method for modeling earthquake dynamics, Journal of Geophysical Research: Solid Earth, 117, 2012.

The HDF Group: Hierarchical Data Format, Version 5, https://www.hdfgroup.org/HDF5/, available at https://github.com/HDFGroup/hdf5.

Uphoff, C. and Bader, M.: Yet another tensor toolbox for discontinuous Galerkin methods and other applications, ACM Transactions on Mathematical Software (TOMS), 46, 1–40, 2020.

Uphoff, C., Rettenberger, S., Bader, M., Madden, E. H., Ulrich, T., Wollherr, S., and Gabriel, A.-A.: Extreme Scale Multi-Physics Simulations of the Tsunamigenic 2004 Sumatra Megathrust Earthquake, in: Proceedings of the International Conference for High Performance Computing, Networking, Storage and Analysis, SC '17, Association for Computing Machinery, New York, NY, USA, ISBN 9781450351140, https://doi.org/10.1145/3126908.3126948, 2017.

Uphoff, C., May, D. A., and Gabriel, A.-A.: A discontinuous Galerkin method for sequences of earthquakes and aseismic slip on multiple faults using unstructured curvilinear grids, Geophysical Journal International, 233, 586–626, 2023.

van Driel, M., Krischer, L., Stähler, S. C., Hosseini, K., and Nissen-Meyer, T.: Instaseis: instant global seismograms based on a broadband waveform database, Solid Earth, 6, 701–717, 2015.

Walker, D. W. and Dongarra, J. J.: MPI: a standard message passing interface, Supercomputer, 12, 56–68, 1996.

Warburton, T.: A low-storage curvilinear discontinuous Galerkin method for wave problems, SIAM Journal on Scientific Computing, 35, A1987–A2012, 2013.

Wilcox, L. C., Stadler, G., Burstedde, C., and Ghattas, O.: A high-order discontinuous Galerkin method for wave propagation through coupled elastic–acoustic media, Journal of Computational Physics, 229, 9373–9396, 2010.

Wilkinson, M. D., Dumontier, M., Aalbersberg, I. J., Appleton, G., Axton, M., Baak, A., Blomberg, N., Boiten, J.-W., da Silva Santos, L. B., Bourne, P. E., et al.: The FAIR Guiding Principles for scientific data management and stewardship, Scientific data, 3, 1–9, 2016.

Yun, J., Gabriel, A.-A., May, D. A., and Fialko, Y.: Controls of dynamic and static stress changes and aseismic slip on delayed earthquake triggering: Application to the 2019 Ridgecrest earthquake sequence, Journal of Geophysical Research: Solid Earth, 130, e2025JB031 271, 2025a.

Yun, J., Gabriel, A.-A., May, D. A., and Fialko, Y.: Effects of stress and friction heterogeneity on spatiotemporal complexity of seismic and aseismic slip on strike-slip faults, Journal of Geophysical Research: Solid Earth, 130, e2025JB031 270, 2025b.

Zhu, W., Allison, K. L., Dunham, E. M., and Yang, Y.: Fault valving and pore pressure evolution in simulations of earthquake sequences and aseismic slip, Nature Communications, 11, 4833, 2020.

Zou, C., Azizzadenesheli, K., Ross, Z. E., and Clayton, R. W.: Deep neural Helmholtz operators for 3-D elastic wave propagation and inversion, Geophysical Journal International, 239, 1469–1484, https://doi.org/10.1093/gji/ggae342, 2024.

Figure Legends

Figure 1. (a) Symmetric Interior Penalty discontinuous Galerkin (SIPG) representation of a SEAS problem. To emphasize the discontinuous nature of the discontinuous Galerkin (DG) representation and the penalty weak coupling across facets, cells and facets are sketched as disjoint; the dashed loops enclose facet basis functions between adjacent cells functions (and across faults) which are collocated in space. (b) Gmsh (Geuzaine and Remacle, 2009) screenshot of a 3D unstructured tetrahedral mesh for the 2019 Ridgecrest, CA, fault system with local refinement near the faults. The element edge length is 250 m at the fault interfaces, gradually coarsening to 20 km toward the domain boundary. This mesh contains 421,154 tetrahedra. (c) 2D unstructured triangular mesh representing the Northern Hikurangi subduction zone, New Zealand (12,160 triangular elements). Colors represent heterogeneous shear modulus (Eberhart-Phillips et al., 2020), which can be represented on the subelement level. (a,b) adapted from Uphoff et al. (2023).

Figure 2. Examples of loading methods for a planar reverse fault model dipping at 30°. Black, grey, and red lines mark the three boundary conditions of `Tandem`, the fault governed by the rate-and-state friction, the free surface, and the Dirichlet boundaries, respectively. Red arrows indicate the imposed displacement vectors along Dirichlet boundaries. Light grey lines show triangular cells with gradually increasing sizes towards the domain boundary.

Figure 3. (a) Weak scaling of an elastostatic solve, on Frontera (TACC, USA), using polynomial degree 4 with varying computational mesh sizes (annotated in red, in million elements). The measured time to solution is shown by the red line, and the ideal weak scaling result is shown by the dashed gray line. The right y-axis is the ratio of ideal CPU time over measured CPU time, with ratio values < 1 indicating better than perfect weak scaling and values > 1 indicating sub-optimal weak scaling. (b) Strong scaling of an elastostatic solve on CPUs (LUMI-C, orange lines) and GPUs (LUMI-G, blue lines), using polynomial degree 4 and a small mesh of 85,492 volume elements. This choice allows `Tandem` to run on a limited number of GPUs on LUMI-G, as larger meshes would exceed the memory capacity of the GPUs, while still providing a meaningful strong-scaling challenge.

Figure 4. `Tandem` results for the SCEC SEAS benchmark BP7 (Lambert et al., 2023). (a) Temporal evolution of slip rate at the center of the velocity-weakening (VW) patch for the slip law. (b) Same as (a) for the aging law. *Tandem* is compared to the boundary-integral code BiCyclE (Lapusta et al., 2000; Lapusta and Liu, 2009) and the finite-difference code Thrase (Erickson and Dunham, 2014). (c) Shear traction on the fault at $t = 0.6$ s. The first rupture is initiated by a smoothly growing stress perturbation starting at $t = 0$ and $(x, z) = (-0.05, -0.05)$ km. (d) Distribution of $(a-b)$ along the fault, with $(a-b) = \pm 0.006$

in the VW and velocity-strengthening (VS) regions, respectively. (e–g) Propagation of the first rupture for the aging law. (h–j) Same as (e–g) for the slip law. Note the different color scales in each panel.

Figure 5. Effects of uniform and depth-varying off-fault elasticity on megathrust earthquake behavior. A – Slip rate along the fault interface for models with uniform (A1) and depth-varying (A2) shear modulus of the domain. B – Shear modulus distribution for the two models. C – Profile of the rate-and-state friction parameter $(b - a)$ used in both models.